PERGAMON

International Journal of Solids and Structures 39 (2002) 393–418

INTERNATIONAL JOURNAL OF SOLIDS and STRUCTURES

www.elsevier.com/locate/ijsolstr

Structural damage identification using piezoelectric sensors

Hisao Fukunaga [a], Ning Hu [a,*], Fu-Kuo Chang [b]

[a] *Department of Aeronautics and Space Engineering, Tohoku University, 01 Aramaki-Aoba, Aoba-ku, Sendai 980-8579, Japan*
[b] *Department of Aeronautics and Astronautics, Stanford University, Stanford, CA 94305, USA*

Received 1 November 2000; in revised form 6 June 2001

Abstract

In this paper, a two-stage damage identification method has been proposed using the data obtained from piezoelectric sensors. In the first stage, a first-order approximation technique is presented for numerically predicting the transient response of electrical potential change on sensors caused by damages. Both numerical and experimental data in the time domain are transformed into the frequency domain using the FFT technique. The damage locations can then be detected by matching the numerical data and the experimental data in the frequency domain through a proposed detection technique. After identifying the possible damage locations, in the second stage, an iterative estimation scheme for solving nonlinear optimization programming problems, based on the quadratic programming technique, is put forward to predict damage extents. A beam example has been employed to illustrate the effectiveness of the algorithm numerically. Furthermore, various investigations, such as the accuracy of the proposed first-order approximation technique, the influences of the excitation frequency of external force, and modelling errors and measurement noises on the results have been carried out.

Keywords: Damage identification; First-order approximation; Piezoelectric sensor; FFT; Inverse problem

1. Introduction

The development of a new class of ''smart'' materials and adaptive structures with sensory/active capabilities may improve the performance and reliability of aeronautical structural systems. Till now, although the applications of actuators and sensors in structural control have received much attention, the researches in the field of damage identification are comparatively limited (Zou et al., 2000). Here some main researches in this field are reviewed briefly. Many researches in this field, till now, have been focused on experimental investigation of the change in the data of piezoelectric sensors due to damages and illustration of the possible detection of the presence of damages. For instance, Luo and Hanagud (1997) have shown the possibility of delamination detection using the nonlinear characteristics of delaminated structures and PVDF sensor sensing properties. Jian et al. (1997) and Penn et al. (1999) have used the vibration data (natural frequency data) from sensors to show the effect of delaminations. They found that the effect of delaminations on the frequency data of thin composite plates is very obvious and decreases rapidly with the

* Corresponding author. Tel.: +81-22-217-4109; fax: +81-22-217-6995.
E-mail address: hu@ssl.mech.tohoku.ac.jp (N. Hu).

0020-7683/01/$ - see front matter
PII: S0020-7683(01)00149-4

increase of plate thickness. Some authors have tried to locate the damages using the piezoelectric sensors. Keilers and Chang (1995a,b) have set up a numerical beam model and employed it with experimental data of frequency response function (FRF) from an attached sensor to identify the delamination location randomly. Banks et al. (1996) put forward a theoretical model for a cantilever beam employing the parameterized partial differential equations and the Galerkin approximation technique. Furthermore, an optimization model solved by a least-square error minimization procedure was proposed for locating the damages using the data of sensors in the time domain. They argued that the data in the time domain are more valuable than those in the frequency domain. Actually, on this topic there has been a long debate. Schulz et al. (1999) have used the transmittance function method to locate the damages with multiple sensors. As they stated, there are some merits using the smart materials for structural health monitoring, such as the continuously on-line or real-time monitoring ability and the comparatively high frequency excitations induced by actuators. Further, Okafor et al. (1996) used the modal data and neural network for delamination detection with built-in piezoelectric sensors in a beam.

It is well known that a major branch in the damage identification is modal based methods. One of the major concerns regarding using the modal analysis to detect damage is that damage is a local phenomenon and modal information is a reflection of the global system properties. Thus, some approaches transform this global information into local information, such as curvatures or strains. From this aspect, it seems that the local information provided by sensors is suitable for damage identification. However, a significant drawback of piezoelectric sensor is just that its data are extremely very limited and localized due to the characteristics of strains. If the sensors are not located in or near the damaged areas, it is difficult to discover the damages because the damages generally have very little or even no influence on the strains of areas, which are far from damaged areas. This may be an important reason for the random search used by Keilers and Chang (1995a,b) even for a simple beam problem. One possible way is to recover the global deformation data from the strain data using the method by Kahl and Sirkis (1996) for a beam. However, this method needs at least to attach the strain gauges onto all sub-sections of the beam. In the current research, a two-stage damage identification method is proposed using limited number of piezoelectric sensors. In the first stage, a first-order approximation technique, which separates the effects of damage severity and damage locations, is proposed to obtain the electrical potential change on sensors in the time domain. In order to detect the damage locations more clearly, both numerical and experimental data in the time domain are transformed into the frequency domain. The damage locations can then be detected by matching the numerical data and the experimental data through a proposed identification technique. This technique combined with the previous first-order approximation can eliminate the influence of damage severity for better detection of damage locations. After obtaining the possible damage locations, in the second stage, an iterative scheme for solving nonlinear optimization programming problems, based on the quadratic programming technique, is proposed to predict damage extents. A beam example is employed to illustrate the effectiveness of the algorithm. The accuracy of the proposed first-order approximation technique has been discussed. The comparison of the damage identification using the data in the time domain and the frequency domain has been carried out. Furthermore, the influences of the excitation frequency of external forces, modelling errors and measurement noises and window methods in the FFT on the results have been investigated in detail.

2. Theory

2.1. Basic assumptions and system equations

The equation of a pre-damaged system can be described as follows:

$$\mathbf{M}\ddot{\mathbf{u}}_0 + \mathbf{K}^0\mathbf{u}_0 = \mathbf{Q} \tag{1a}$$

$$\boldsymbol{\phi}_S^0 = -\mathbf{S}\mathbf{u}_0 \tag{1b}$$

where $\mathbf{M}$ is the mass matrix, $\ddot{\mathbf{u}}_0$ is the system acceleration vector, $\mathbf{u}_0$ is the displacement vector, $\mathbf{K}^0$ is the effective stiffness matrix, $\mathbf{Q}$ represents the mechanical force or actuator force vector and $\boldsymbol{\phi}_S^0$ is the vector of electrical potential on sensors. Also, $\mathbf{K}^0$ and $\mathbf{S}$ will be briefly described in Appendix A.

The equation of a damaged system can also be cast into the following similar form:

$$\mathbf{M}\ddot{\mathbf{u}}_1 + (\mathbf{K}^0 + \Delta\mathbf{K})\mathbf{u}_1 = \mathbf{Q} \tag{2a}$$

$$\boldsymbol{\phi}_S^1 = -\mathbf{S}\mathbf{u}_1 \tag{2b}$$

where damages are considered as a perturbation of the stiffness matrix, i.e., $\Delta\mathbf{K}$.

Generally, damping is also very sensitive to structural damages. For instance, increase in damping due to damages in composite materials was reported to be many fold (Chandra et al., 1999). Then, it is possible to employ the change of damping as measure of damage. However, general speaking, damping often has too low influence on dynamic responses. In this study, for the sake of simplicity, the damping is neglected.

From Eqs. (1a)–(2b), it can be seen that the task of damage identification is to search for the damage location and to estimate the damage extents by analysing the difference between $\boldsymbol{\phi}_S^0$ and $\boldsymbol{\phi}_S^1$. Generally, the response of damaged structures is a nonlinear function of damage location and damage extent, i.e., $\boldsymbol{\phi}_S^1(\alpha, \mathbf{P})$, where α is the damage extent and $\mathbf{P}$ is a vector representing the damage positions. For the sake of simplicity, the effect of damage extent is simplified by a scalar α. It is usually difficult to identify two parameters simultaneously due to very limited data and coupled effects of two parameters. We try to separate the influences of two parameters in order to search for the damage location more easily. Performing the Taylor expansion of $\boldsymbol{\phi}_S^1(\alpha, \mathbf{P})$ to α leads to

$$\boldsymbol{\phi}_S^1(\alpha, \mathbf{P}) \approx \boldsymbol{\phi}_S^0 + \alpha\mathbf{A}_1(\mathbf{P}) + \alpha^2\mathbf{A}_2(\mathbf{P}) + \cdots \tag{3}$$

where $\mathbf{A}_1$, $\mathbf{A}_2$, ... are only functions of damage locations.

This is the fundamental assumption in this research, i.e., the effects of damage extent and damage location can be separated approximately. This assumption is reasonable. For instance, Cawley and Adams (1979) showed that the ratio of frequency changes in different modes is only a function of damage location and not the magnitude of damage. Our previous experimental research (Wang et al., 2001) also showed that the ratio of frequency changes and displacement changes is only a function of damage location. From Eq. (3), the electrical potential change can be expressed as,

$$\Delta\boldsymbol{\phi}_S(\alpha, \mathbf{P}) \approx \alpha\mathbf{A}_1(\mathbf{P}) + \alpha^2\mathbf{A}_2(\mathbf{P}) + \cdots \tag{4}$$

A technique for damage detection is proposed later to eliminate the influence of α when only the first-order approximation is used. The first-order approximation may be inaccurate for computing high damage extents. However, it can be used for detection of damage locations if the main features of structural response can be captured.

2.2. First-order approximation

By employing the modal superposition method, the transient response $\mathbf{u}_0(t)$ of the pre-damaged system can be expanded as follows:

$$\mathbf{u}_0(\mathbf{x}, t) = \sum_{i=1}^{N} \boldsymbol{\varphi}_i(\mathbf{x}) x_i^0(t) \tag{5}$$

where $\mathbf{x}$ denotes the spatial position of a particle. Re-writing Eq. (1a) in the modal space results into

$$\ddot{x}_i^0(t) + \omega_i^2 x_i^0(t) = \boldsymbol{\varphi}_i^{\mathrm{T}} \mathbf{Q}(t) \tag{6}$$

where $\boldsymbol{\varphi}_i$ and ω_i are the mode and frequency of undamaged structure, i.e., $\mathbf{K}^0 \boldsymbol{\varphi}_i = \omega_i^2 \mathbf{M} \boldsymbol{\varphi}_i$. In derivation of Eq. (6), the following conditions are employed although the normalization in Eq. (7b) may be unnecessary in the current approach,

$$\boldsymbol{\varphi}_i^{\mathrm{T}} \mathbf{K}^0 \boldsymbol{\varphi}_i = \omega_i^2 \ \text{ and } \ \boldsymbol{\varphi}_i^{\mathrm{T}} \mathbf{K}^0 \boldsymbol{\varphi}_j = 0 \quad (i \neq j) \tag{7a}$$

$$\boldsymbol{\varphi}_i^{\mathrm{T}} \mathbf{M} \boldsymbol{\varphi}_i = 1 \ \text{ and } \ \boldsymbol{\varphi}_i^{\mathrm{T}} \mathbf{M} \boldsymbol{\varphi}_j = 0 \quad (i \neq j) \tag{7b}$$

Under condition of the harmonic input for $\mathbf{Q}(\tau)$, especially for the case of sinusoidal input, i.e., $\mathbf{p} \sin(\omega_f \tau)$, where $\mathbf{p}$ is a vector ($\in \mathscr{R}^{n \times 1}$ and n is the degrees of freedom of system) denoting the positions and amplitudes of loads, Eq. (6) can be solved from Duhamel's integral for zero initial conditions as follows:

$$x_i^0(t) = \frac{\boldsymbol{\varphi}_i^{\mathrm{T}} \mathbf{p}}{\omega_i} \int_0^t \sin(\omega_f \tau) \sin \omega_i (t - \tau) \mathrm{d}\tau = \frac{\boldsymbol{\varphi}_i^{\mathrm{T}} \mathbf{p}}{\omega_i} F_i(t) \tag{8}$$

where the integral $F_i(t)$ can be described in the following form:

$$F_i(t) = \frac{-\sin(\omega_f t)\omega_i + \sin(\omega_i t)\omega_f}{(\omega_f + \omega_i)(\omega_f - \omega_i)} \tag{9}$$

Furthermore, Eq. (2a) can also be expanded in the modal space as follows:

$$\ddot{x}_i^1(t) + \overline{\omega}_i^2 x_i^1(t) = \overline{\boldsymbol{\varphi}}_i^{\mathrm{T}} \mathbf{Q}(t) \tag{10}$$

where $\overline{\omega}_\imath$ and $\overline{\boldsymbol{\varphi}}_i$ are the natural frequency and vibration mode of damaged structure. The solution of Eq. (10) can be obtained in the same way as stated above

$$x_i^1(t) = \frac{\overline{\boldsymbol{\varphi}}_i^{\mathrm{T}} \mathbf{p}}{\overline{\omega}_i} F_i^*(t) \ \text{ and } \ F_i^*(t) = \frac{-\sin(\omega_f t)\overline{\omega}_i + \sin(\overline{\omega}_i t)\omega_f}{(\omega_f + \overline{\omega}_i)(\omega_f - \overline{\omega}_i)} \tag{11}$$

In the above equation, the response of damaged structure is obviously a nonlinear function of structural modal data. By employing the following perturbations:

$$\overline{\omega}_i = \omega_i + \Delta\omega_i \ \text{ and } \ \overline{\boldsymbol{\varphi}}_i = \boldsymbol{\varphi}_i + \Delta\boldsymbol{\varphi}_i \tag{12}$$

and neglecting the higher-order terms, such as $(\Delta\omega_i/\omega_i)^2$, $(\Delta\boldsymbol{\varphi}_i^{\mathrm{T}})^2$ and $(\Delta\boldsymbol{\varphi}_i^{\mathrm{T}} \Delta\omega_i/\omega_i)$ in the expansion, $x_i^1(t)$ in Eq. (11) can be finally approximated as

$$x_i^1(t) \approx \frac{\boldsymbol{\varphi}_i^{\mathrm{T}} \mathbf{p}}{\omega_i} F_i(t) + \frac{\Delta\boldsymbol{\varphi}_i^{\mathrm{T}} \mathbf{p}}{\omega_i} F_i(t) + \frac{\boldsymbol{\varphi}_i^{\mathrm{T}} \mathbf{p}}{\omega_i} F_i'(t) \left(\frac{\Delta\omega_i}{\omega_i} \right) \tag{13}$$

where

$$F_i'(t) = -\frac{\sin(\omega_f t)\omega_i(\omega_f^2 + \omega_i^2)}{(\omega_f^4 - 2\omega_f^2\omega_i^2 + \omega_i^4)} + \frac{\omega_f \omega_i [\cos(\omega_i t) t(\omega_f^2 - \omega_i^2) + 2\sin(\omega_i t)\omega_i]}{(\omega_f^4 - 2\omega_f^2\omega_i^2 + \omega_i^4)} + \frac{\sin(\omega_f t)\omega_i - \omega_f \sin(\omega_i t)}{(\omega_f + \omega_i)(\omega_f - \omega_i)} \tag{14}$$

There is $\cos(\omega_i t)t$ in the numerator of the second term of Eq. (14), which is nonharmonic. Actually, this term is obtained from $\sin(\overline{\omega}_i t)$ in the second term of the numerator of $F_i^*(t)$ in Eq. (11) because there is

$$\sin(\overline{\omega}_i t) = \sin(\omega_i t + \Delta\omega_i t) = \sin(\Delta\omega_i t)\cos(\omega_i t) + \sin(\omega_i t)\cos(\Delta\omega_i t) \approx \Delta\omega_i t \cos(\omega_i t) + \sin(\omega_i t) \tag{15}$$

The displacements of damaged structure can also be expressed as

$$\mathbf{u}_1(\mathbf{x},t)=\sum_{i=1}^{N}\overline{\boldsymbol{\varphi}}_i(\mathbf{x})x_i^1(t) \tag{16}$$

From Eqs. (5), (8), (13) and (16), the change of displacement caused by damages is

$$\Delta\mathbf{u}=\mathbf{u}_0-\mathbf{u}_1\approx\sum_{i=1}^{N}\left[-\Delta\boldsymbol{\varphi}_i\frac{\boldsymbol{\varphi}_i^{\mathrm{T}}\mathbf{p}}{\omega_i}F_i(t)-\boldsymbol{\varphi}_i\frac{\Delta\boldsymbol{\varphi}_i^{\mathrm{T}}\mathbf{p}}{\omega_i}F_i(t)-\boldsymbol{\varphi}_i\frac{\boldsymbol{\varphi}_i^{\mathrm{T}}\mathbf{p}}{\omega_i}F_i'(t)\left(\frac{\Delta\omega_i}{\omega_i}\right)\right] \tag{17}$$

The above equation is the most important formulation in this research. In fact, this equation relates the changes of transient responses in the time domain, i.e., the left hand side, to the modal data, i.e., the right hand side. In the right hand side, the first two terms represent the changes of displacement caused by the variation of vibration mode. The third term represents the changes of displacement caused by the changes of natural frequency. Furthermore, by observing Eq. (9), it can be found that $F_i(t)$ is a harmonic function. Then, in Eq. (17), the influences of variation of vibration mode on the transient response are harmonic. However, the term of $\cos(\omega_i t)t$ in $F_i'(t)$ of Eq. (14) is nonharmonic. Therefore, the influences of change of natural frequency on the transient response, i.e., the third term of Eq. (17), are nonharmonic in the first-order approximation. As stated later, the influence of the third term on transient responses is much more significant than those of the first two terms. The above closed-form equation for the first-order approximation makes the computation cost very low and can also be used in other areas, such as for re-analysis in general optimum design.

Following the work of Stetson (1975), the first-order perturbation is used to relate $\Delta\omega_i$ and $\Delta\boldsymbol{\varphi}_i$ with $\Delta\mathbf{K}$. Under condition of stiffness change only, the changes in natural frequency and mode can be described as follows:

$$\Delta\omega_i\approx\frac{1}{2}\left(\frac{\Delta k_i}{\omega_i}\right) \tag{18a}$$

$$\Delta\boldsymbol{\varphi}_i=\sum_{j=1}^{M}\frac{\Delta k_{ij}}{(\omega_i^2-\omega_j^2)}\boldsymbol{\varphi}_j,\quad i\neq j \tag{18b}$$

where

$$\Delta k_i=\boldsymbol{\varphi}_i^{\mathrm{T}}\Delta\mathbf{K}\boldsymbol{\varphi}_i \tag{19a}$$

$$\Delta k_{ij}=\boldsymbol{\varphi}_i^{\mathrm{T}}\Delta\mathbf{K}\boldsymbol{\varphi}_j \tag{19b}$$

Eq. (18b) is only suitable for problems in which there are different natural frequencies. If a system possesses multiple eigenfrequencies (eigenvalues), the change of mode relating to the eigenfrequencies is indefinite. We will discuss this problem later.

Finally, from Eqs. (1b), (17)–(19b), the potential change can be expressed as

$$\Delta\boldsymbol{\phi}_{\mathrm{S}}\approx\mathbf{S}\left\{\sum_{i=1}^{N}\left[-\sum_{j=1}^{M}\frac{\boldsymbol{\varphi}_i^{\mathrm{T}}\Delta\mathbf{K}\boldsymbol{\varphi}_j}{(\omega_i^2-\omega_j^2)\omega_i}\boldsymbol{\varphi}_j\boldsymbol{\varphi}_i^{\mathrm{T}}\mathbf{p}F_i(t)-\sum_{j=1}^{M}\frac{\boldsymbol{\varphi}_i^{\mathrm{T}}\Delta\mathbf{K}\boldsymbol{\varphi}_j}{(\omega_i^2-\omega_j^2)\omega_i}\boldsymbol{\varphi}_i\boldsymbol{\varphi}_j^{\mathrm{T}}\mathbf{p}F_i(t)-\frac{\boldsymbol{\varphi}_i^{\mathrm{T}}\Delta\mathbf{K}\boldsymbol{\varphi}_i}{2\omega_i^3}\boldsymbol{\varphi}_i\boldsymbol{\varphi}_i^{\mathrm{T}}\mathbf{p}F_i'(t)\right]\right\},\quad i\neq j \tag{20}$$

2.3. Identification technique for damage location

When using the finite element method (FEM), the stiffness change $\Delta\mathbf{K}$ in system can be expressed as the summation of the changes in elemental stiffness matrices as follows:

$$\Delta\mathbf{K} = \sum_{i=1}^{\mathrm{ND}} \mathbf{B}_i^{\mathrm{T}} \Delta\mathbf{k}_i^* \mathbf{B}_i \tag{21}$$

where ND is the number of damaged elements, $\mathbf{B}_i$ is the Boolen matrix of element i and $\Delta\mathbf{k}_i^*$ is the stiffness change of element i, which can further be expressed as

$$\Delta\mathbf{k}_i^* = \alpha_i \Delta\mathbf{k}_i \tag{22}$$

where α_i is a scalar denoting the damage fraction or damage extent ($-1.0 \leqslant \alpha_i \leqslant 0.0$) and $\Delta\mathbf{k}_i$ is the stiffness matrix of undamaged element i. For structures with single damage or multiple damages with the same severity, the scalar α_i can be extracted out in Eq. (21) (denoted by α) for separating the effects of damage extent and damage location.

The electrical potential change on sensor l can be calculated from Eq. (20),

$$\Delta\boldsymbol{\phi}_{\mathrm{S}}^{l}(t) \approx \mathbf{S}_l \sum_{i=1}^{N} \left[-\sum_{j=1}^{M} \frac{\boldsymbol{\varphi}_i^{\mathrm{T}} \sum_{k=1}^{\mathrm{ND}} \alpha_k \mathbf{B}_k^{\mathrm{T}} \Delta\mathbf{k}_k \mathbf{B}_k \boldsymbol{\varphi}_j}{(\omega_i^2 - \omega_j^2)\omega_i} \boldsymbol{\varphi}_j \boldsymbol{\varphi}_i^{\mathrm{T}} \mathbf{p} F_i(t) - \sum_{j=1}^{M} \frac{\boldsymbol{\varphi}_i^{\mathrm{T}} \sum_{k=1}^{\mathrm{ND}} \alpha_k \mathbf{B}_k^{\mathrm{T}} \Delta\mathbf{k}_k \mathbf{B}_k \boldsymbol{\varphi}_j}{(\omega_i^2 - \omega_j^2)\omega_i} \boldsymbol{\varphi}_i \boldsymbol{\varphi}_j^{\mathrm{T}} \mathbf{p} F_i(t) \right.$$
$$\left. - \frac{\boldsymbol{\varphi}_i^{\mathrm{T}} \sum_{k=1}^{\mathrm{ND}} \alpha_k \mathbf{B}_k^{\mathrm{T}} \Delta\mathbf{k}_k \mathbf{B}_k \boldsymbol{\varphi}_i}{2\omega_i^3} \boldsymbol{\varphi}_i \boldsymbol{\varphi}_i^{\mathrm{T}} \mathbf{p} F_i'(t) \right], \quad i \neq j \tag{23}$$

where $\mathbf{S}_l$ is the lth row of $\mathbf{S}$ matrix.

If we assume that the damage exists in one element only, i.e., ND = 1, the comparison between the numerical estimation in Eq. (23) and the corresponding experimental results $\Delta\boldsymbol{\phi}_{\mathrm{S}}^{l^*}(t)$ in the time domain can be carried out one element by one element sequentially. However, as shown in our later numerical verifications, this comparison can be performed more effectively when transforming the data from the discrete time domain to the frequency domain using the following FFT,

$$\Delta\boldsymbol{\Phi}_{\mathrm{S}}^{l}[k] = \sum_{n=0}^{L-1} \Delta\boldsymbol{\phi}_{\mathrm{S}}^{l}[n] w[n] \mathrm{e}^{-j(2\pi/L)k\cdot n} \tag{24}$$

where $w[n]$ is a window function to eliminate the effects of discontinuity and higher-order frequency. Generally there are many window methods, such as Blackman window, Hanning window, Hamming window etc. (Oppenheim and Schafer, 1989).

Generally, the various quantities obtained from the FFT can be employed for damage identification, here the spectrum radius, i.e., $\left\|\mathrm{Re}(\Delta\boldsymbol{\Phi}_{\mathrm{S}}^{l}) + \mathrm{j}\,\mathrm{Im}(\Delta\boldsymbol{\Phi}_{\mathrm{S}}^{l})\right\|$ is used, which is also represented by $\Delta\boldsymbol{\Phi}_{\mathrm{S}}^{l}$ thereafter for simplicity. Then, the simplest comparison between the measured results and the numerically estimated results in the frequency domain can be carried out as follows:

$$\Delta\boldsymbol{\Phi}_{\mathrm{S}}^{l}(f_j) \approx \Delta\boldsymbol{\Phi}_{\mathrm{S}}^{l^*}(f_j) \tag{25}$$

where f_j is a frequency sampling point within the frequency domain and $\Delta\boldsymbol{\Phi}_{\mathrm{S}}^{l^*}(f_j)$ is the experimental data in the frequency domain. However, a major difficulty using Eq. (25) is that we do not know the damage extent and cannot predict $\Delta\boldsymbol{\Phi}_{\mathrm{S}}^{l}(f_j)$ accurately. Therefore, we can only compare the similarity or likelihood between two curves of different amplitudes in the frequency domain. From a different point of view, the following normalized correlation of the scale invariance is defined

$$\rho(\Delta\boldsymbol{\Phi}_{\mathrm{S}}^{l}, \Delta\boldsymbol{\Phi}_{\mathrm{S}}^{l^*}) = \frac{\Delta\boldsymbol{\Phi}_{\mathrm{S}}^{l} \cdot \Delta\boldsymbol{\Phi}_{\mathrm{S}}^{l^*}}{\left\|\Delta\boldsymbol{\Phi}_{\mathrm{S}}^{l}\right\| \left\|\Delta\boldsymbol{\Phi}_{\mathrm{S}}^{l^*}\right\|} \tag{26}$$

where $\Delta\boldsymbol{\Phi}_{\mathrm{S}}^{l}$ and $\Delta\boldsymbol{\Phi}_{\mathrm{S}}^{l^*}$ are vectors with components $\Delta\boldsymbol{\Phi}_{\mathrm{S}}^{l}(f_j)$ and $\Delta\boldsymbol{\Phi}_{\mathrm{S}}^{l^*}(f_j)$. When the above correlation is close to 1, then two vectors are very similar. The possibility of the occurrence of damage in the corresponding element is high. From Eq. (22), it can be seen that α, i.e., the damage extent can be eliminated in

Eq. (26). Then, Eq. (26) keeps only the information of damage location. Setting the number of sensors NSE for comparison, for element i, the following equation is employed

$$E_i = \sum_{l=1}^{\mathrm{NSE}} |1 - \rho_i(\Delta\boldsymbol{\Phi}_{\mathrm{S}}^{l}|_i, \Delta\boldsymbol{\Phi}_{\mathrm{S}}^{l^*})| \tag{27}$$

where $\Delta\boldsymbol{\Phi}_{\mathrm{S}}^{l}|_i$ is the numerically generated data when assuming damage in element i.

The possible damage location is then indicated by the smallest discrepancy calculated from Eq. (27). The following parameter D_i is defined for element i:

$$D_i = \frac{1}{E_i} \tag{28}$$

The largest one of D_i corresponds to the possible damaged member. Therefore, the following damage index is finally defined for element i:

$$\mathrm{DAM}_i = \frac{D_i}{\mathrm{MAX}(D_j,\ j = 1, 2, \ldots, \mathrm{NE})} \tag{29}$$

where NE is the number of elements in structure.

Actually, the normalized correlation in Eq. (26) may also reduce the influence of errors caused by the first-order approximation compared with Eq. (25). By checking the right hand side in Eq. (26), from Eq. (4) for simplicity it can be expressed as follows:

$$\frac{\Delta\boldsymbol{\Phi}_{\mathrm{S}}^{l} \cdot \Delta\boldsymbol{\Phi}_{\mathrm{S}}^{l^*}}{\|\Delta\boldsymbol{\Phi}_{\mathrm{S}}^{l}\|\|\Delta\boldsymbol{\Phi}_{\mathrm{S}}^{l^*}\|} = \frac{A_1\alpha + A_2\alpha^2 + A_3\alpha^3 + \cdots}{B_1\alpha + B_2\alpha^2 + B_3\alpha^3 + \cdots} \approx \frac{A_1}{B_1} + \frac{A_2B_1 - A_1B_2}{B_1^2}\alpha + \cdots \tag{30}$$

The error in the above formulation when using the first-order approximation, i.e., the relative error between $(A_1\alpha + A_2\alpha^2 + A_3\alpha^3 + \cdots)/(B_1\alpha + B_2\alpha^2 + B_3\alpha^3 + \cdots)$ and A_1/B_1 is $(A_2 - D)\alpha/A_1$, where $D = A_1B_2/B_1$. For the numerator only in Eq. (30), if the first-order approximation is used, the error, i.e., the relative error between $A_1\alpha + A_2\alpha^2 + A_3\alpha^3 + \cdots$ and $A_1\alpha$ is $A_2\alpha/A_1$. In the frequency domain, the positive spectrum radius is used. Therefore, B_1 and A_1 are negative due to negative α. Also it is easy to verify that A_2 and B_2 are of the same sign (in fact they are of the almost same order considering the spectrum radius used here). Then, from the Cauchy inequality, we can obtain $|B_1| \geqslant |A_1|$. Therefore, generally $|A_2 - D|$ is smaller than $|A_2|$, and errors from the first-order approximation in Eq. (26) are reduced.

The above identification procedure can also be employed in the time domain by replacing $\Delta\boldsymbol{\Phi}_{\mathrm{S}}^{l}(f)$ and $\Delta\boldsymbol{\Phi}_{\mathrm{S}}^{l^*}(f)$ with $\Delta\boldsymbol{\phi}_{\mathrm{S}}^{l}(t)$ and $\Delta\boldsymbol{\phi}_{S}^{l^*}(t)$ in Eq. (26).

There are two important characteristics in the current method. The first one is about the types of damage that the analysis is applicable to. In Eqs. (4) and (22), where the damage extent is represented by a scalar α, then it is assumed that the damage affects the stiffness by the same proportion in all directions. For instance, for one dimensional problems (e.g. a beam), the surface transverse crack (Wang et al., 2001) causing the reduction of bending rigidity, belongs to this case. For two dimensional structures, the damage of a hole in an isotropic material (Cawley and Adams, 1979; Banks et al., 1996) would be this case. Also, for two dimensional structures of anisotropic materials, the damage by crushing, which includes many small randomly oriented microcracks, can also be approximated using this type of damage (Cawley and Adams, 1979). However, the assumption is no longer valid with a macro/directional crack or damage in two dimensional or three dimensional structures, which causes the different changes of stiffness in the different directions. The second one is that the model of damage used assumes that the damage is at one site only because we search for the possible damaged area one element by one element. From our previous experiences (Wang et al., 2001), for multiple damages, the present method can only roughly identify the area of the highest damage severity or its adjacent area.

2.4. Estimation of damage extent

When the possible damaged members are detected by employing the above technique, the estimation of damage extent is the next important step. It is hoped that the undamaged members in the possible damaged members detected in the first step can be removed. Furthermore, the investigation of damage extent in damaged members can provide some important information about the structural safety.

The current algorithm is based on the minimization of a least-squared error function, which has the following general form for one sensor, where the variables $\boldsymbol{x}$ are linearly constrained between bounds:

$$\begin{aligned} &\min \quad J(\boldsymbol{x}) = \tfrac{1}{2}\|\boldsymbol{e}(\boldsymbol{x})\|^2 \\ &\text{s.t.} \quad \underline{\boldsymbol{x}} \leqslant \boldsymbol{x} \leqslant \overline{\boldsymbol{x}} \end{aligned} \tag{31}$$

where $\boldsymbol{e}(\boldsymbol{x})$ is a measure of discrepancy between an observation and its counterpart computed by the parameterized model.

Here, for the sake of simplicity, the data in the time domain are used. For sensor l, the measure of error is the difference between the electrical potential change computed from the FEM model and its measured counterpart of the real structure, i.e., $\boldsymbol{e}(\boldsymbol{\alpha}) = \Delta\boldsymbol{\phi}_{\mathrm{S}}^{l}(t_n) - \Delta\boldsymbol{\phi}_{\mathrm{S}}^{l^*}(t_n)$, $n = 1, \ldots, \mathrm{NS}$, where NS is the number of sampling points in the time domain. The design variable vector $\boldsymbol{\alpha}$ includes the damage extents of all possible damaged elements detected in the first step.

If there are NP possible damaged members, from Eq. (23) we can obtain:

$$\Delta\boldsymbol{\phi}_{\mathrm{S}}^{l}(t) \approx \sum_{m=1}^{\mathrm{NP}} \alpha_m Z_m \tag{32}$$

where

$$\begin{aligned} Z_m(t) = \mathbf{S}_l \sum_{i=1}^{N} \Bigg[&- \sum_{j=1}^{M} \frac{\boldsymbol{\varphi}_i^{\mathrm{T}} \mathbf{B}_m^{\mathrm{T}} \Delta\mathbf{k}_m \mathbf{B}_m \boldsymbol{\varphi}_j}{(\omega_i^2 - \omega_j^2)\omega_i} \boldsymbol{\varphi}_j \boldsymbol{\varphi}_i^{\mathrm{T}} \mathbf{p} F_i(t) - \sum_{j=1}^{M} \frac{\boldsymbol{\varphi}_i^{\mathrm{T}} \mathbf{B}_m^{\mathrm{T}} \Delta\mathbf{k}_m \mathbf{B}_m \boldsymbol{\varphi}_j}{(\omega_i^2 - \omega_j^2)\omega_i} \boldsymbol{\varphi}_i \boldsymbol{\varphi}_j^{\mathrm{T}} \mathbf{p} F_i(t) \\ &- \frac{\boldsymbol{\varphi}_i^{\mathrm{T}} \mathbf{B}_m^{\mathrm{T}} \Delta\mathbf{k}_m \mathbf{B}_m \boldsymbol{\varphi}_i}{2\omega_i^3} \boldsymbol{\varphi}_i \boldsymbol{\varphi}_i^{\mathrm{T}} \mathbf{p} F_i'(t) \Bigg], \quad i \neq j \end{aligned} \tag{33}$$

Then, from Eq. (31), the final optimization model can be cast into the following quadratic programming problem:

$$\begin{aligned} &\min \quad f(\boldsymbol{\alpha}) = \tfrac{1}{2}\boldsymbol{\alpha}^{\mathrm{T}} \mathbf{A} \boldsymbol{\alpha} + \mathbf{C}^{\mathrm{T}} \boldsymbol{\alpha} + D \\ &\text{s.t.} \quad -\mathbf{d} \leqslant \mathbf{I}\boldsymbol{\alpha} \leqslant \mathbf{0} \end{aligned} \tag{34}$$

where

$$\boldsymbol{\alpha} = \{\alpha_1, \alpha_2, \ldots, \alpha_{\mathrm{NP}}\} \tag{35a}$$

$$\mathbf{A} = \begin{bmatrix} \sum_{n=1}^{\mathrm{NS}} (Z_1^n)^2 & \sum_{n=1}^{\mathrm{NS}} Z_1^n Z_2^n & \cdots & \sum_{n=1}^{\mathrm{NS}} Z_1^n Z_{\mathrm{NP}}^n \\ \sum_{n=1}^{\mathrm{NS}} Z_2^n Z_1^n & \sum_{n=1}^{\mathrm{NS}} (Z_2^n)^2 & \cdots & \sum_{n=1}^{\mathrm{NS}} Z_2^n Z_{\mathrm{NP}}^n \\ \vdots & \vdots & \vdots & \vdots \\ \sum_{n=1}^{\mathrm{NS}} Z_{\mathrm{NP}}^n Z_1^n & \sum_{n=1}^{\mathrm{NS}} Z_{\mathrm{NP}}^n Z_2^n & \cdots & \sum_{n=1}^{n} (Z_{\mathrm{NP}}^n)^2 \end{bmatrix} \tag{35b}$$

$$\mathbf{C}^{\mathrm{T}} = \left\{ -\sum_{n=1}^{\mathrm{NS}} Z_1^n \Delta\boldsymbol{\phi}_{\mathrm{S}}^{l^{*n}} \quad -\sum_{n=1}^{\mathrm{NS}} Z_2^n \Delta\boldsymbol{\phi}_{\mathrm{S}}^{l^{*n}} \quad \cdots \quad -\sum_{n=1}^{\mathrm{NS}} Z_{\mathrm{NP}}^n \Delta\boldsymbol{\phi}_{\mathrm{S}}^{l^{*n}} \right\} \tag{35c}$$

$$D = \sum_{n=1}^{\mathrm{NS}} \left(\Delta\boldsymbol{\phi}_{\mathrm{S}}^{l^{*n}} \right)^2 \tag{35d}$$

where the superscript n means that the quantity is evaluated at t_n in the time domain. Also, $\mathbf{d}$, $\mathbf{0}$ and $\mathbf{I}$ are a vector with all components of unit value, a vector with all components of zero, and unit diagonal matrix, respectively.

The algorithm presented by Goldfarb and Idnani (1983) is adopted to deal with this quadratic programming problem. Although the above formulations are constructed for the data of only one sensor, it is not difficult to extend it for the data of multiple sensors. The constrained optimization problem in Eq. (31) is intrinsically nonlinear, and the first-order approximation in Eq. (32) is introduced to linearize it. However, if the absolute value of α_i is not small enough, the precision of linear approximation cannot be guaranteed. Then, the following iterative process is employed to correct the above standard algorithm.

Step 1: Initialize – Initialize the variables, vectors and matrixes that will be utilized. Start with a working set that there is no damage in the structure:

$$\Delta\mathbf{K}^0 = \mathbf{0} \tag{36a}$$

$$\boldsymbol{\alpha}^0 = \Delta\boldsymbol{\alpha}^0 = \mathbf{0} \tag{36b}$$

Step 2: Solve quadratic programming problem – Calculate the change of stiffness matrix $\Delta\mathbf{K}^{i-1}$ according to the current increment of damage extent $\Delta\boldsymbol{\alpha}^{i-1}$, which is used to replace the unknowns $\boldsymbol{\alpha}$ in Eqs. (34)–(35d). Add up the iteration index ($i = i + 1$), and update the stiffness matrix:

$$\mathbf{K}^i = \mathbf{K}^{i-1} + \Delta\mathbf{K}^{i-1} \tag{37}$$

Use $\mathbf{K}^i$ to carry out a new eigenvalue computation and update $\boldsymbol{\varphi}_j$ and ω_j. Introduce into $\delta(\Delta\boldsymbol{\phi}_{\mathrm{S}}^{l^*})^i$, which is expressed as follows, to replace $\Delta\boldsymbol{\phi}_{\mathrm{S}}^{l^*}$ in Eqs. (35c) and (35d).

$$\delta(\Delta\boldsymbol{\phi}_{\mathrm{S}}^{l^*})^i = \Delta\boldsymbol{\phi}_{\mathrm{S}}^{l^*} - (\Delta\overline{\boldsymbol{\phi}}_{\mathrm{S}}^{l})^i \tag{38}$$

Use updated $\boldsymbol{\varphi}_j$ and ω_j to construct new $Z_m(t)$, $\mathbf{A}$ matrix and $\mathbf{D}$ vector, then solve the quadratic programming problem (34) to get the increment of damage extent $\Delta\boldsymbol{\alpha}^i$. In Eq. (38), $\Delta\boldsymbol{\phi}_{\mathrm{S}}^{l^*}$ is the electrical potential changes experimentally acquired, and $(\Delta\overline{\boldsymbol{\phi}}_{\mathrm{S}}^{l})^i = (\boldsymbol{\phi}_{\mathrm{S}}^{l})^0 - (\boldsymbol{\phi}_{\mathrm{S}}^{l})^i$, where $(\boldsymbol{\phi}_{\mathrm{S}}^{l})^i$ and $(\boldsymbol{\phi}_{\mathrm{S}}^{l})^0$ are electrical potentials computed from $\mathbf{K}^i$ and $\mathbf{K}^0$, respectively.

Step 3: Evaluate the discrepancy of the linear approximation – Update the damage extents as follows:

$$\boldsymbol{\alpha}^i = \boldsymbol{\alpha}^{i-1} + \Delta\boldsymbol{\alpha}^i \tag{39}$$

If $\Delta\boldsymbol{\alpha}^i$ is less than a pre-set threshold, it can be considered that the obtained damage extent $\boldsymbol{\alpha}^i$ is sufficiently close to the real value, then terminate the analysing procedure. Otherwise, go back to step 2. Naturally, the constraint conditions in Eq. (34) for $\boldsymbol{\alpha}$ should be changed in terms of $\boldsymbol{\alpha}^{i-1}$ and $\Delta\boldsymbol{\alpha}^i$.

3. Numerical examples

A beam shown in Fig. 1 is employed to investigate the effectiveness of the proposed identification algorithm. The propped cantilever beam is chosen here arbitrarily although the current method has been verified to be effective for other structures, such as cantilever beam. The materials constants of composite plate of 0° plies only are listed as: $E_{11} = 142.0$ GPa, $E_{22} = 10.3$ GPa, $G_{12} = G_{13} = 7.2$ GPa, $G_{23} = 4.29$ GPa, $\nu_{12} = 0.25$ and $\rho = 1382.1$ kg/m^3, where "1" and "2" denote the x-axis direction and the y-axis direction, respectively. The mechanical and piezoelectric properties of PVDF sensor are: $E_{11} = E_{22} = E_{33} = 2.0$ GPa, $G_{12} = G_{13} = G_{23} = 0.8$ GPa, $\nu_{12} = \nu_{23} = \nu_{13} = 0.25$, $d_{31} = -154.0$ pm/V, $d_{32} = 0.0$ pm/V, $p_{33} = 0.1505 \times 10^{-9}$ F/m and $\rho = 1300.0$ kg/m^3. Only the bending deformation in the x-axis direction is considered. The in-plane deformation, the bending deformation in the y-axis direction and the torsional deformation are neglected for the sake of simplicity. Our previously proposed nine-node element using a higher-order plate

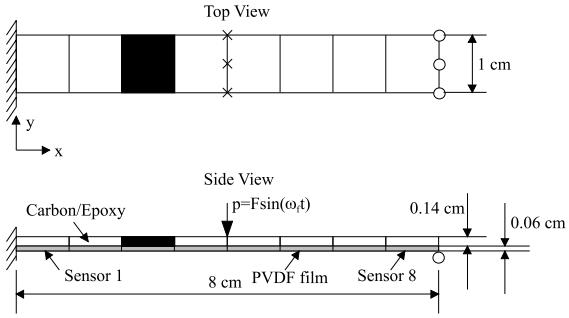

Fig. 1. Geometry of a beam with an attached piezoelectrics layer.

Table 1
Natural frequency of a beam

	1	2	3	4	5	6	7
ω (rad/s)	3206.448	9711.978	18 500.737	28 545.475	31 260.393	32 634.059	35 179.090
f (Hz)	510.322	1545.709	2944.484	4543.153	4975.246	5193.872	5598.926

theory (Fukunaga et al., in press) is employed and degrees of freedom of system for the mechanical field are 141. The first seven natural frequencies of beam are shown in Table 1. The frequency of three identical concentrated external forces, i.e., ω_f is 22 000 rad/s, which is located between the third and fourth circular natural frequencies of beam. The amplitude of the concentrated forces is 50 N. The damage is assumed to occur at element 3 with the reduction in the elastic modulus. As stated previously, we should use the same reduction proportion representing damage for all tension and shear module (i.e., E_{11}, E_{22}, G_{12}, G_{13} and G_{23}). Then, the damage extent α can be extracted from an orthotropic elastic matrix as that in Eq. (22) and then can be eliminated finally in Eq. (26). In the following computation, the time increment step is 2 μs, and N and M in Eq. (20) for modal superposition are 50.

3.1. Comparison of the static and dynamical response of sensors

At first, for various damage extents, the electrical potentials of sensors under the static load are plotted in Fig. 2. In this figure, only the electrical potential on sensor 3 under the damaged element, changes significantly. The electrical potentials of other sensors have almost not changed. Therefore, it is very difficult to identify the damages using the static data if the sensor is not located in the damaged areas because the data of sensor can only reflect the local stiffness change caused by damage. Moreover, from this figure, it can be found that element 3 carries relatively low strain energy, then it is a relatively difficult case for identification. Under the dynamical load, the electrical potential changes on sensors 3 and 6 are shown in Figs. 3 and 4, respectively. Both figures show the significant changes. With the increase of time, the changes become more obviously. Therefore, unlike the static case, it is possible to use the data obtained from a sensor, which is not located in the damaged areas, to identify the damage.

3.2. Discussion on accuracy of the first-order approximation

To check the accuracy of the first-order approximation, the change of central deflection of beam is employed as shown in Fig. 5. In this figure, two kinds of first-order approximation approaches are em-

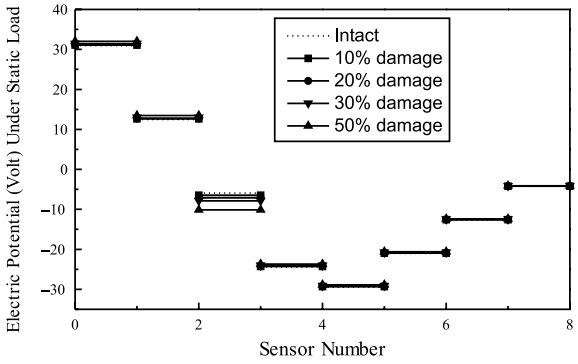

Fig. 2. Electrical potential change under static loads.

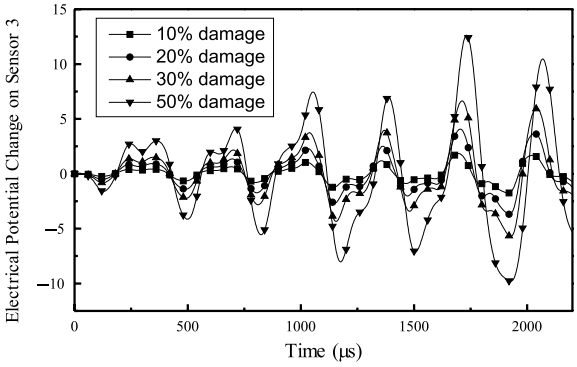

Fig. 3. Electrical potential change on sensor 3 under dynamical loads.

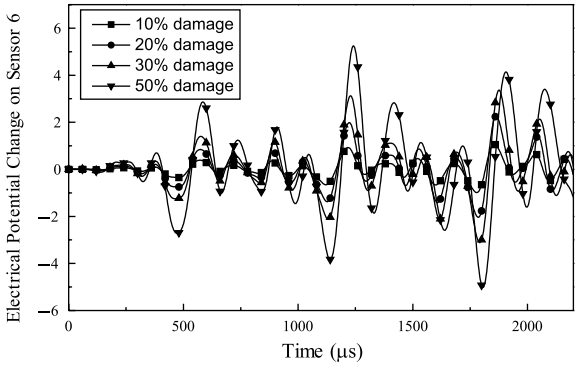

Fig. 4. Electrical potential change on sensor 6 under dynamical loads.

ployed. FODA1 denotes that all three terms are used in Eq. (17) and FODA2 denotes that only the third term in Eq. (17) is used. Then, in FODA2, the contribution of changes of vibration mode is ignored. Inspection of this figure reveals that the first-order approximation has quite high accuracy even for 30% damage extent. For 50% damage extent, the accuracy of the first-order approximation decreases. The

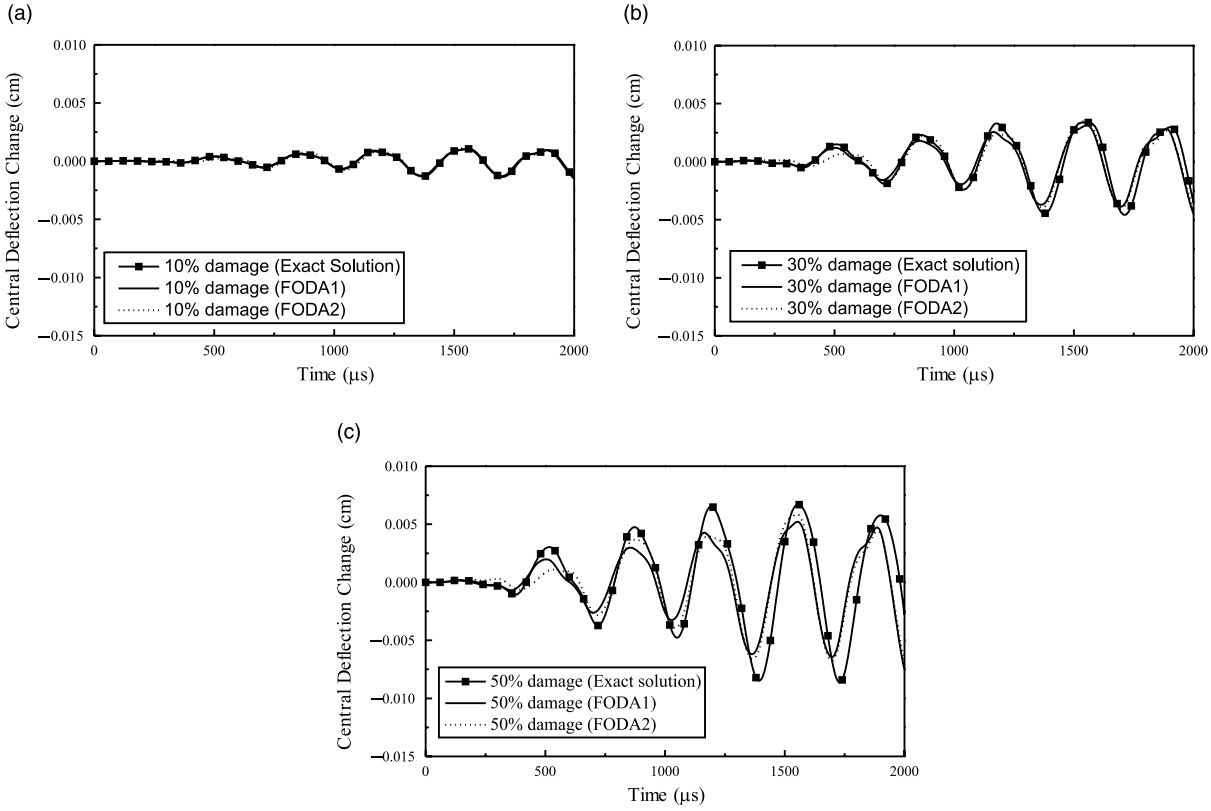

Fig. 5. Comparison between exact central deflection change and that predicted by first-order approach: (a) 10% damage, (b) 30% damage and (c) 50% damage.

accuracy of FODA2 is only a little lower than that of FODA1 within an initial time period. Therefore, compared with the effect of changes of natural frequency, the contribution of changes of vibration mode is small. In fact, Weissenburger (1968) has shown that the mode shapes do not change much as local stiffness or mass is modified. Also, Chance et al. (1994) showed that the mode shapes of a damaged system and that of an undamaged system are nearly the same. Armon et al. (1994) also assumed that mode shapes remain unchanged by the small change in stiffness. Stubbs (1987) even pointed out that they are exactly the same if the damage is uniform. Then, for some structures with multiple eigenfrequencies, such as symmetrical structures, the changes of vibration mode for these frequencies are indefinite. In this case, the following two procedures can be taken simultaneously. One is to choose the frequency of external force to be far from multiple eigenfrequencies since the structural transient response is mainly dominated by the modal data of the natural frequencies, which are close to the frequency of external force. Another is that, in the first two terms of Eq. (17), the contribution of changes of vibration modes for multiple eigenfrequencies is neglected, but the contribution of changes of vibration modes of single frequency is kept. Furthermore, in the third term, the contribution of all modes should be considered.

3.3. Discussion on data of time domain and frequency domain

When the damage extent is low, due to the high accuracy of the first-order approximation, usually the damage identification, i.e., Eq. (26) can also be used in the time domain. However, the problem arises for

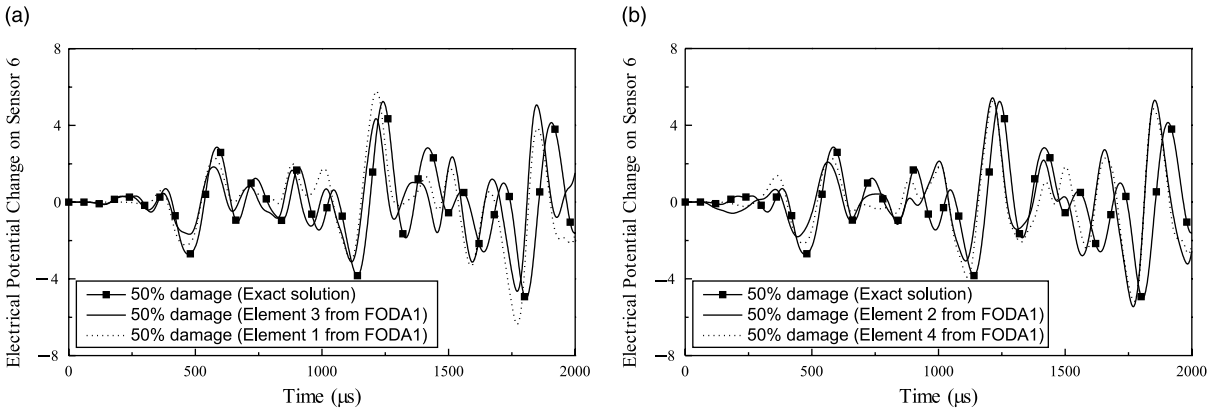

Fig. 6. Comparison between exact electrical potential change on sensor 6 and that predicted by first-order approach: (a) 50% damage in elements 1 and 3, respectively and (b) 50% damage in elements 2 and 4, respectively.

seriously damaged cases. For instance, for 50% damage in element 3, by employing the data in the time domain obtained from the sensors far away from the damage area, such as 6, 7 and 8, we found that the possibilities of damage in elements 1, 2 and 4 (D_i in Eq. (28)) are also very high using Eq. (26) although the highest possibility of damage still appears in element 3. To explain the reason, the results of the potential change on sensor 6 are shown in Fig. 6 when assuming the damage in elements 1, 2, 3 and 4, respectively. Fig. 6 shows that it is very difficult to distinguish which one in the results of elements 1, 2, 3 and 4 is more similar to the exact result, especially between the results of element 1 and element 3.

To overcome this problem, the data in the time domain are transformed into the frequency domain using Eq. (24). Our numerical experiences have shown that the application of window methods in FFT, such as Blackman window or Hanning window, can lead to obviously better results even for numerically simulated experimental data. When using practical experimental data with high noises, the window methods may be more helpful. Fig. 7 shows the spectrum radius of potential change on sensor 6 in FFT using Blackman window when assuming the damage in elements 1, 2, 3 and 4, respectively. Note that the negative frequency domain in this figure is only the result of FFT transformation on the mathematical meaning, not on the physical meaning. Inspection of this figure reveals that the result of element 3 is most similar to the exact solution although the amplitude is different. Here, we emphasize on curve shape, not scale or size, since practically we have no information about the damage extent. The curve shapes for elements 1, 2 and 4 in the frequency domain are completely different from the exact solution. From Fig. 7, it can be concluded that the first-order approximation can capture the main features of potential change in the frequency domain. Furthermore, through the use of the first-order approximation, the influence of damage extent is completely extracted out and separated from the influence of damage location. For instance, Fig. 7(f) shows the result using Blackman window when assuming 10% damage in element 3. By comparing Fig. 7(f) with 7(b) of 50% damage case, it can be found that the shapes of two curves are completely identical except the different amplitudes or scales.

The data shown in Fig. 7 are different from the usual FRF data used by other authors, such as Schulz and Thyagarajian (1995), Keilers and Chang (1995a,b) and Wang et al. (1997) from following several respects. First, here the FFT transformation is performed on the data of electrical potential change in the time domain. Therefore, the obtained data in the frequency domain contain the integrated modal information (especially natural frequency information) of both undamaged and damaged structures, i.e., the changes in natural frequency and mode due to damages. Inversely, the usual FRF data used by other authors are only for the undamaged or damaged structures independently. Second, for a prescribed excitation frequency of

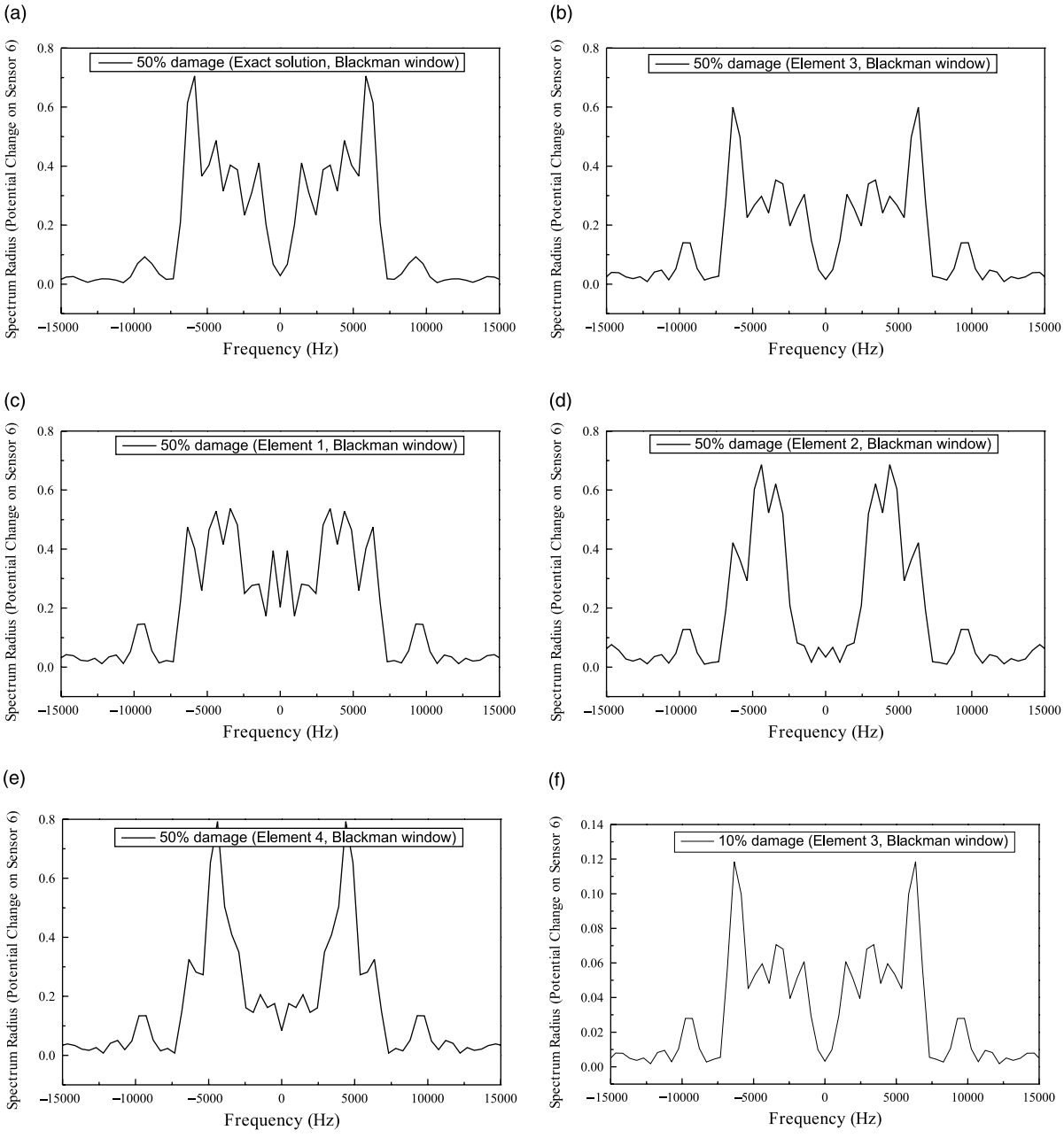

Fig. 7. (a) Spectrum radius of exact electrical potential change on sensor 6 (50% damage). Spectrum radius of electrical potential change on sensor 6 predicted by first-order approximation (b) 50% damage in element 3, (c) 50% damage in element 1, (d) 50% damage in element 2, (e) 50% damage in element 4 and (f) 10% damage in element 3.

external force, the present data contain the information of those modal data whose natural frequencies are close to the excitation frequency. For instance, because the excitation frequency is located between the third and fourth natural frequencies here, Fig. 7(a) contains the information of the first several modal data and

their changes by observing Table 1. However, in the usual FRF under harmonic excitation, it contains the information of one frequency point only. For instance, when the frequency of harmonic excitation is equal to a natural frequency, the resonance occurs and only the modal data corresponding to that natural frequency can be obtained. Third, to obtain the usual FRF curves numerically, one needs to scan over the whole frequency domain where he is interested. Then it is computationally very expensive. For example, if one needs to obtain the frequency responses at 100 frequency points, he has to perform 100 inverse computation of a large-scale equation with components of complex number (Schulz and Thyagarajian, 1995). However, only the analysis of transient response using Eq. (23) and one FFT analysis are needed here, whose computational costs are comparatively very low.

In the present analysis, the sufficient long sampling time domain should be taken in order to guarantee the accuracy of FFT transformation and include the sufficient modal data. Our numerical experiences have shown that the time domain should be at least taken up to $T_1 = 1/f_1$ for obtaining stable results in the frequency domain, where f_1 is the fundamental frequency of structures. Of course, too long time domain may decrease the accuracy of Eq. (15).

3.4. Results of damage location identification

When using Eq. (26), the frequency domain is taken from -6840 to 6840 Hz. Twenty nine sampling points within this frequency domain are used. The results of damage detection for 10% damage case are illustrated in Fig. 8 when using the data of sensor 1, sensor 6 and sensor 8, independently. Fig. 8 shows that the damage location can be detected very successfully. When using data of other sensors, the damage can also be detected very clearly. Of course, the location of sensor has certain influences on the final results.

We also computed Eq. (26) in the time domain. The time domain is chosen from 100 to 2000 μs, and the number of sampling points is 951. Fig. 9 shows the results when using the data of sensor 1 and 8, respectively. Comparing with Fig. 8(a) and (c), it can be seen that the results in Fig. 9 become worse, especially for sensor 8.

When the damage extent in element 3 is up to 50%, the identification results are shown in Fig. 10. Inspection of this figure reveals that the results become worse (especially for sensor 8) due to the errors introduced in the first-order approximation, although the damage location can be identified.

3.5. Effect of excitation frequency of external force

To investigate the influence of the frequency of external force, we change the frequency of external force ω_f from 22 000 to 3000 rad/s, which is lower than the 1st circular natural frequency. When using the data of sensor 1, 6 and 8 independently, the results for 10% and 50% damage cases are shown Figs. 11 and 12, respectively. From these figures, it can be found that the damage location can be identified more clearly, especially when using the data of sensor 8 for 50% damage case. We drop ω_f again from 3000 to 1000 rad/s, it was found that the damage can also be identified although the results become only a little worse compared with those of 3000 rad/s. However, the results of 1000 rad/s are better than those of 22 000 rad/s. Also, we computed the results when increasing ω_f from 22 000 rad/s to a higher level, e.g. 33 000 rad/s. It was found that the damage can also be located successfully. However, the results become a little worse compared with those of 22 000 rad/s. Therefore, it can be pointed out that the present algorithm is not sensitive to the frequency of external force. However, the better results can be obtained when the frequency of external force is around or even lower than the 1st circular natural frequency in the present example.

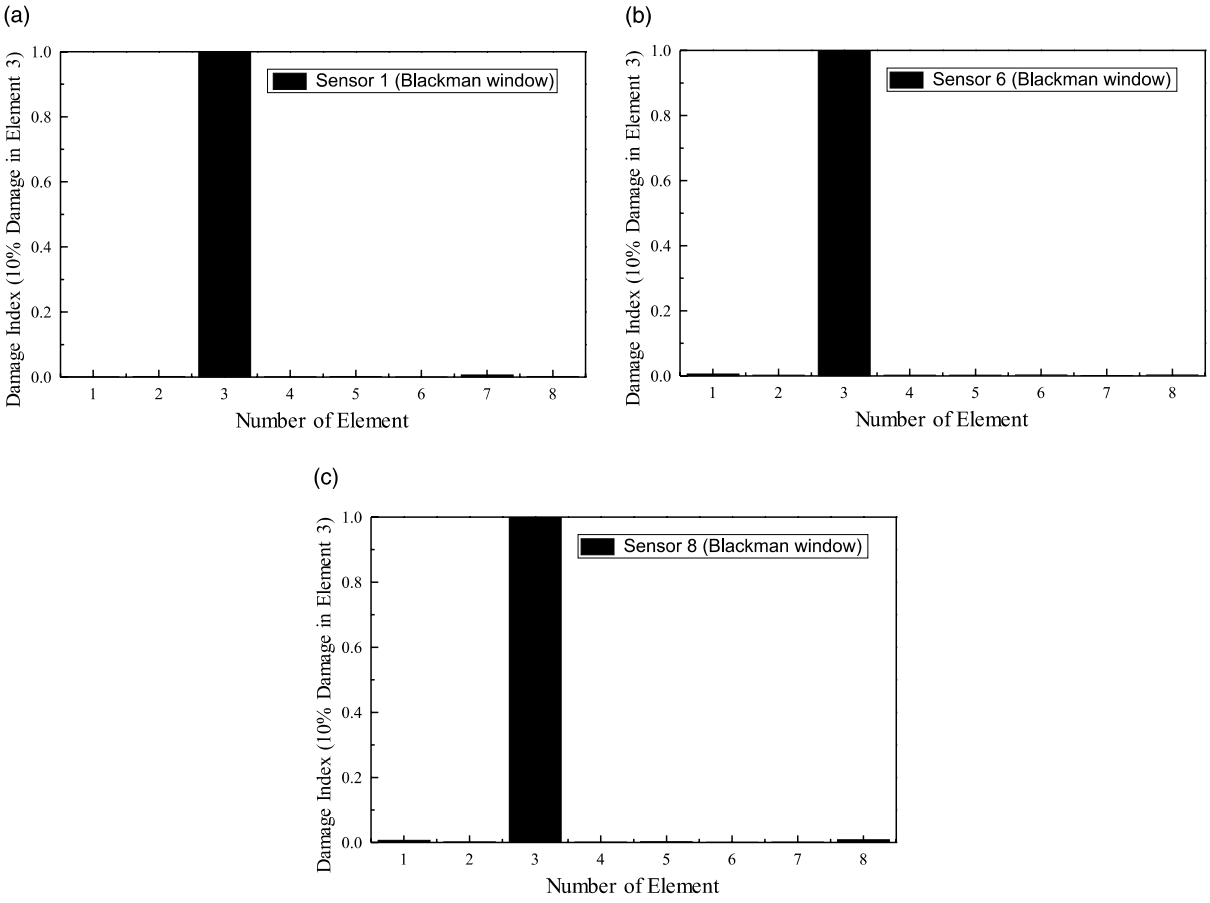

Fig. 8. Damage location using data on (a) sensor 1 (10% damage), (b) sensor 6 (10% damage), and (c) sensor 8 (10% damage).

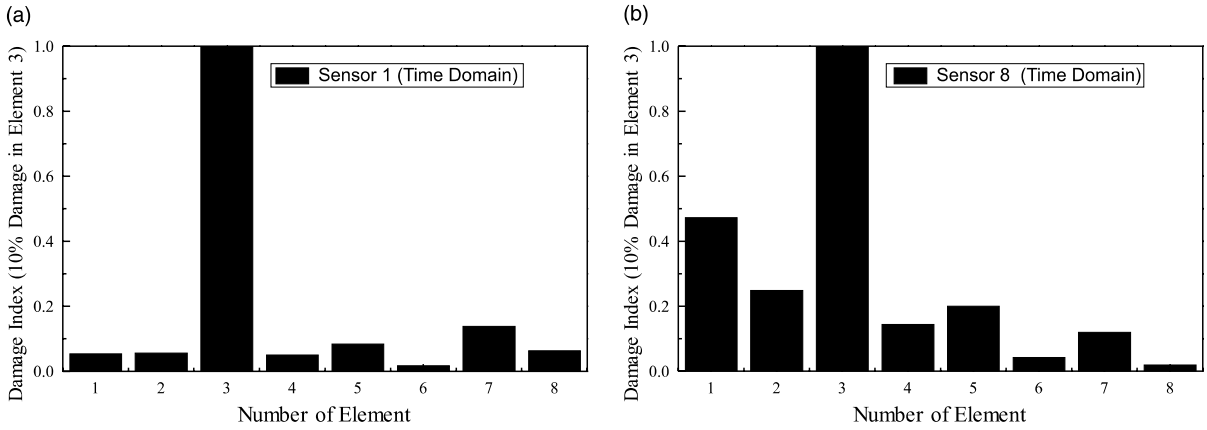

Fig. 9. Damage location using data on (a) sensor 1 in time domain (10% damage) and (b) sensor 8 in time domain (10% damage).

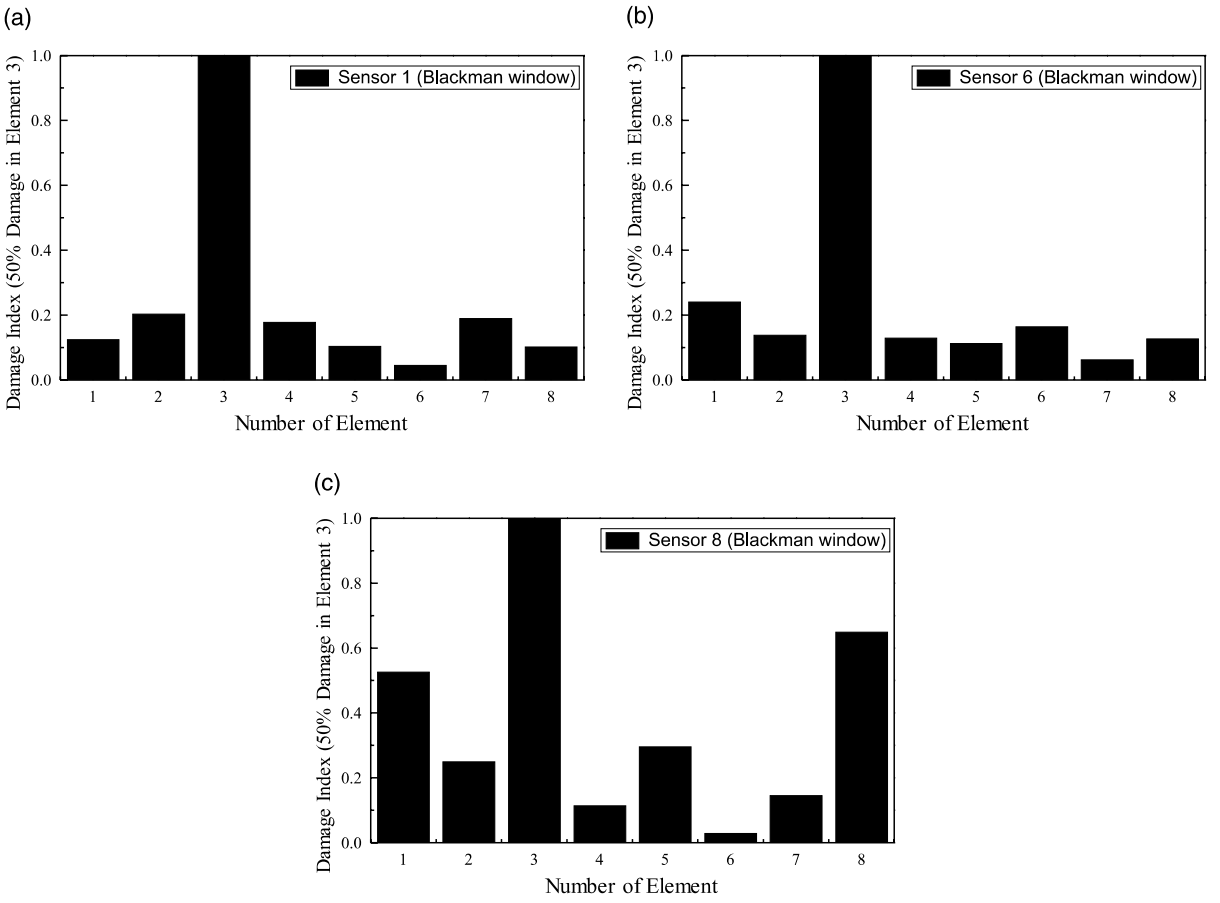

Fig. 10. Damage location using data on (a) sensor 1 (50% damage), (b) sensor 6 (50% damage), and (c) sensor 8 (50% damage).

3.6. Effect of modelling error and measurement noise

To investigate the robustness of the present technique, the numerical modelling errors and experimental measurement noises are simulated in three steps in the present researches, which are shown in Fig. 13. The first step is to simulate the period elongation due to the disregard of some factors in numerical modelling, such as damping. The original data in the time domain are first elongated with ΔT (50 μs) as shown in Fig. 13 (note the fundamental period of beam is 1959 μs Table 1). The second step is to enlarge the response in the time domain as shown in Fig. 13 to simulate the uncertainties of boundary conditions and material constants. In Fig. 13, ΔA is set as $0.05\Delta\boldsymbol{\phi}_{\mathrm{S}}^{l}(t)$, i.e., 5.0% increase corresponding to the amplitude of electrical potential change in the time domain. The third step is to simulate the higher frequency noises from electrical measurement devices. The random noise (white noise with zero mean value) is simulated with the level of 2% of $(\Delta\boldsymbol{\phi}_{\mathrm{S}}^{l}(t) + 0.05\Delta\boldsymbol{\phi}_{\mathrm{S}}^{l}(t))$, which is added over the electrical potential change after step 2. After obtained the contaminated experimental data in the time domain, the FFT transformation is performed and the damage location is identified. When ω_f is selected as 3000 rad/s, the corresponding results are shown in Figs. 14 and 15 for 10% and 50% damage cases, respectively. Comparing these figures with Figs. 11 and 12, no obvious influences from the added high level noises and great modelling errors can be identified. The damage location can also be detected clearly, and the robustness of the present technique is quite high.

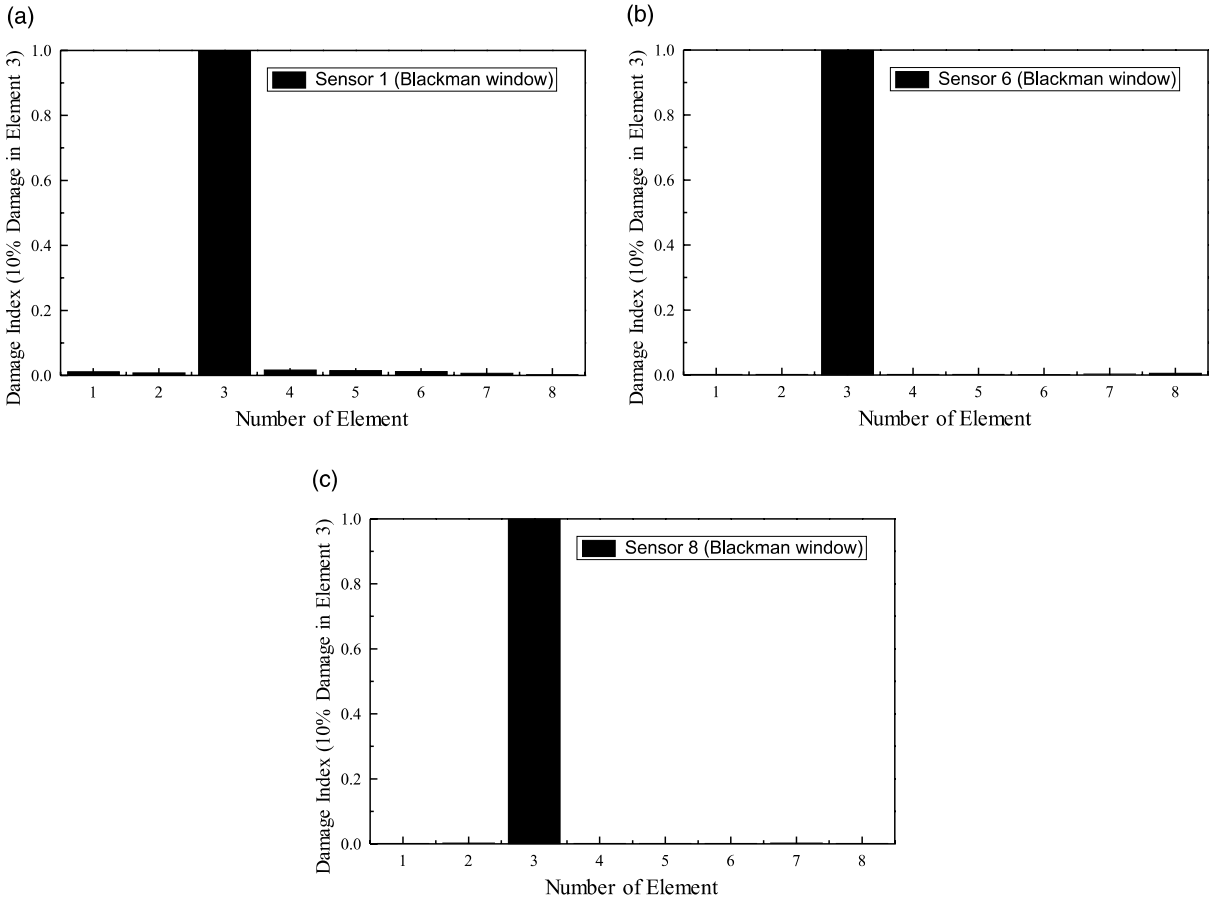

Fig. 11. Damage location using data on (a) sensor 1 (low excitation frequency and 10% damage), (b) sensor 6 (low excitation frequency and 10% damage), and (c) sensor 8 (low excitation frequency and 10% damage).

3.7. Results of damage extent

Finally, the damage extent is calculated using the nonlinear least-square algorithm stated previously. ω_f is equal to 3000 rad/s. 1100 sampling points (i.e., NS) in the time domain from 0 to 2200 μs are used. For 10% damage case, the results of damage extent are shown in Table 2 when using the data of three sensors, independently. The possible damaged element is chosen as element 3 by observing Fig. 11. Table 2 shows that good results can be obtained. The convergence history is shown in Fig. 16(a) in which only two or three iterations are needed before convergence. The results for 50% damage case are shown in Table 3, in which three sets of possible damaged elements are chosen to check the effectiveness of the present nonlinear least-square technique. In the first set, only element 3 is chosen and the corresponding convergence history is shown in Fig. 16(b). Table 3 shows that good results can be obtained. In the second set, by observing Fig. 12, we chose three possible damaged elements as shown in Table 3. From this table, it can be found that the damage extent in element 3 can be obtained accurately and two undamaged elements can be distinguished from 3 candidates due to their low damage extents. Finally, we chose all 8 elements as candidates. The results in Table 3 shows that the damage extent in element 3 can also be predicted accurately and other elements can be removed from the candidates. This example shows that the present analysis procedure is

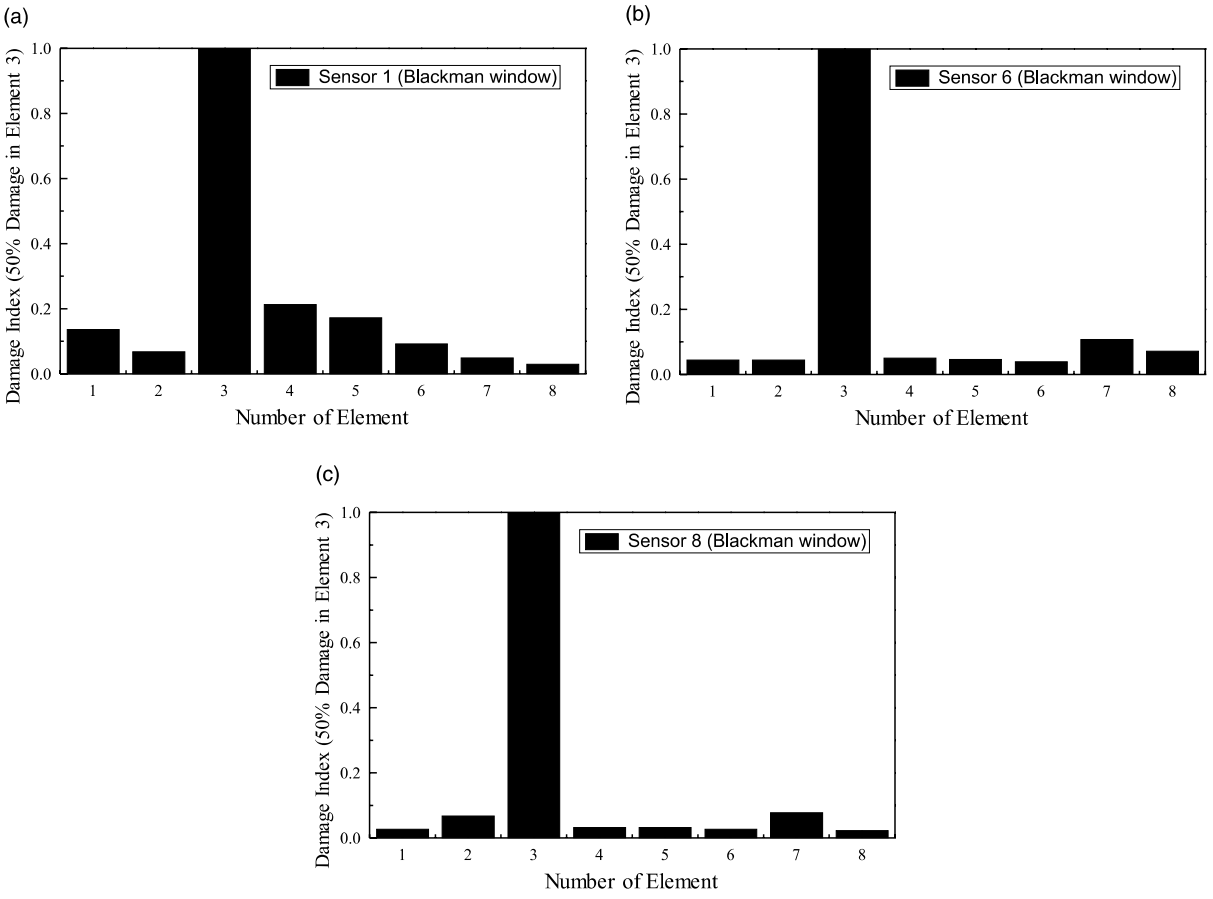

Fig. 12. Damage location using data on (a) sensor 1 (low excitation frequency and 50% damage), (b) sensor 6 (low excitation frequency and 50% damage), and (c) sensor 8 (low excitation frequency and 50% damage).

effective although only the data from one sensor are employed. Naturally, when using practically measured data, it is difficult to obtain the accurate damage extents due to the influence of noises and modelling errors. Also, for complex structures, it is not practical to choose all elements as candidates to perform the nonlinear least-square computation. Therefore, the detection of damage location in the first stage is crucial to reduce the number of possible damaged elements and increase computational efficiency.

4. Conclusions

In this paper, a two-stage damage identification method using the limited number of piezoelectric sensors (actually only one sensor is employed here) has been proposed. In the first stage, a first-order approximation technique is proposed for obtaining the transient response of electrical potential changes on sensors. After the FFT transformation of the numerical and experimental data from the time domain to the frequency domain, an identification technique for damage locations is proposed by matching the numerical data and the experimental data. After obtaining the possible damage locations, in the second stage, an iterative estimation scheme for solving nonlinear optimization programming problems is presented to

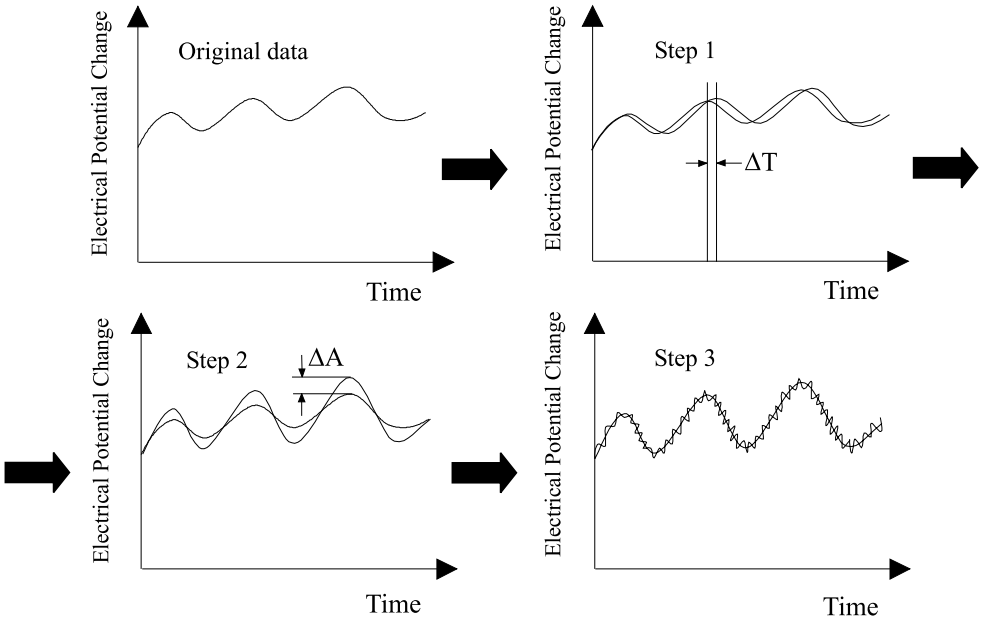

Fig. 13. Flowchart for adding modelling error and measurement noise into data.

predict damage extents. A beam example is employed to illustrate the effectiveness of the present algorithm. From the numerical example, it was found that the accuracy of the first-order approximation technique is high. The damage identification results using the data in the frequency domain are better than those using the data in the time domain. The window methods used in the FFT are helpful for enhancing the identification accuracy. Furthermore, the influences of the frequency of external force, and modelling errors and measurement noises on the identification results are not obvious. Naturally, the current approach has its own drawbacks, such as the strong dependence on the reliable modal data of undamaged structure for obtaining a reasonable first-order approximation in Eq. (20). Also, for complicated structures, its effectiveness needs to be further investigated numerically and experimentally. This paper just shows a possible direction of the application of piezoelectric sensors for damage identification.

Appendix A

In this paper, the finite element computation is carried out based on a nine-node higher-order plate element proposed by the authors (Fukunaga et al., in press). In this element, the following third-order displacement fields have been adopted:

$$u(x,y,z) = u_0 + z\left[\theta_x - \frac{4}{3}\left(\frac{z}{h}\right)^2\left(\theta_x + \frac{\partial w}{\partial x}\right)\right] \tag{A.1}$$

$$v(x,y,z) = v_0 + z\left[\theta_y - \frac{4}{3}\left(\frac{z}{h}\right)^2\left(\theta_y + \frac{\partial w}{\partial y}\right)\right] \tag{A.2}$$

$$w(x,y) = w_0 \tag{A.3}$$

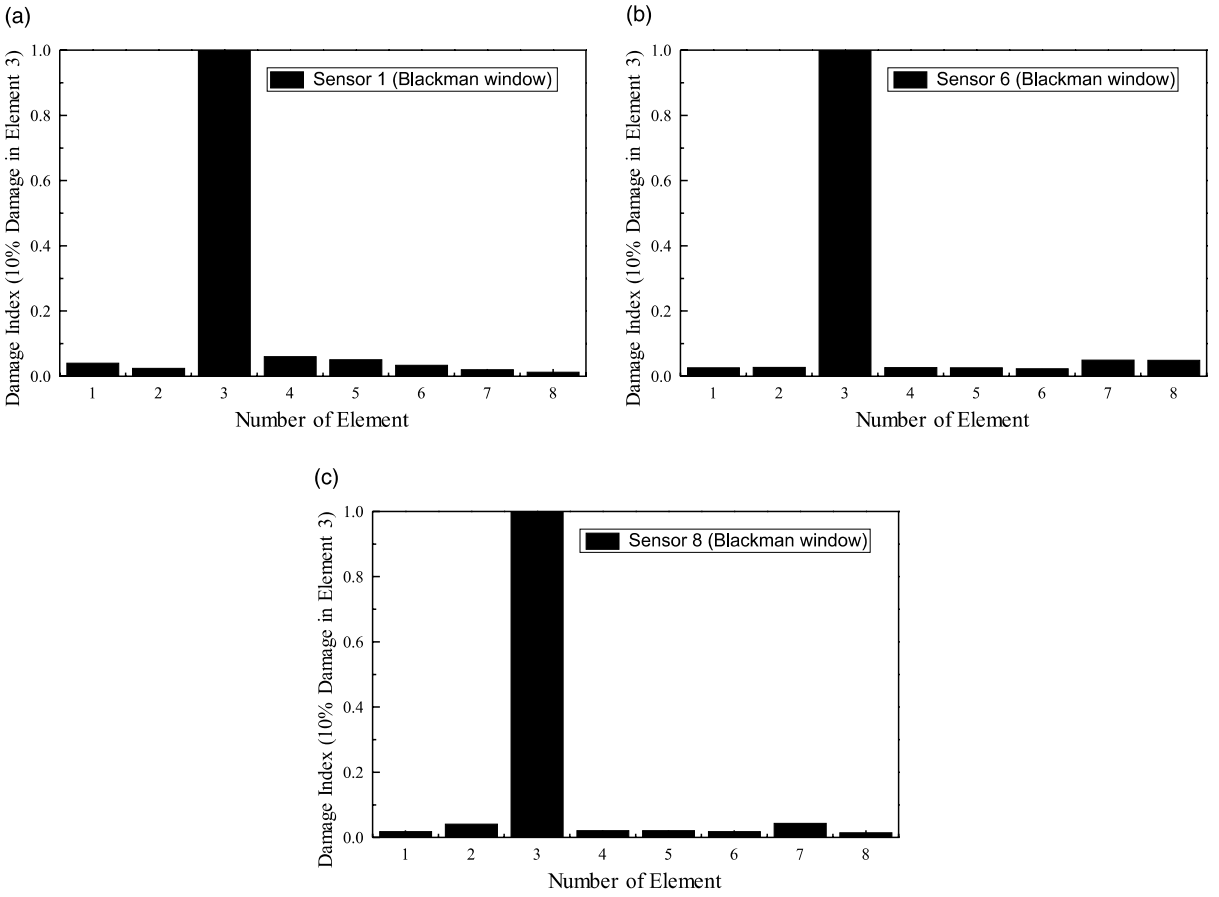

Fig. 14. Damage location using contaminated data on (a) sensor 1 (10% damage), (b) sensor 6 (10% damage), and (c) sensor 8 (10% damage).

where u_0, v_0 and w_0 are the displacements on the mid-plane, θ_x and θ_y are the rotations due to shear deformation about the y and x axes respectively and h is the thickness of plate. This displacement field satisfies free conditions of the transverse shear strains on the top and bottom surfaces of plate, i.e., $\varepsilon_{xz}(x, y, \pm(h/2)) = 0$ and $\varepsilon_{yz}(x, y, \pm(h/2)) = 0$.

The strains associated with the displacements in Eqs. (A.1)–(A.3) can be described as

$$\varepsilon_x(x, y, z) = \varepsilon_x^0 + z(\kappa_x^0 + z^2\kappa_x^1) \tag{A.4}$$

$$\varepsilon_y(x, y, z) = \varepsilon_y^0 + z(\kappa_y^0 + z^2\kappa_y^1) \tag{A.5}$$

$$\varepsilon_{xy}(x, y, z) = \varepsilon_{xy}^0 + z(\kappa_{xy}^0 + z^2\kappa_{xy}^1) \tag{A.6}$$

$$\varepsilon_{yz}(x, y, z) = \varepsilon_{yz}^0 + z^2\kappa_{yz}^1 \tag{A.7}$$

$$\varepsilon_{xz}(x, y, z) = \varepsilon_{xz}^0 + z^2\kappa_{xz}^1 \tag{A.8}$$

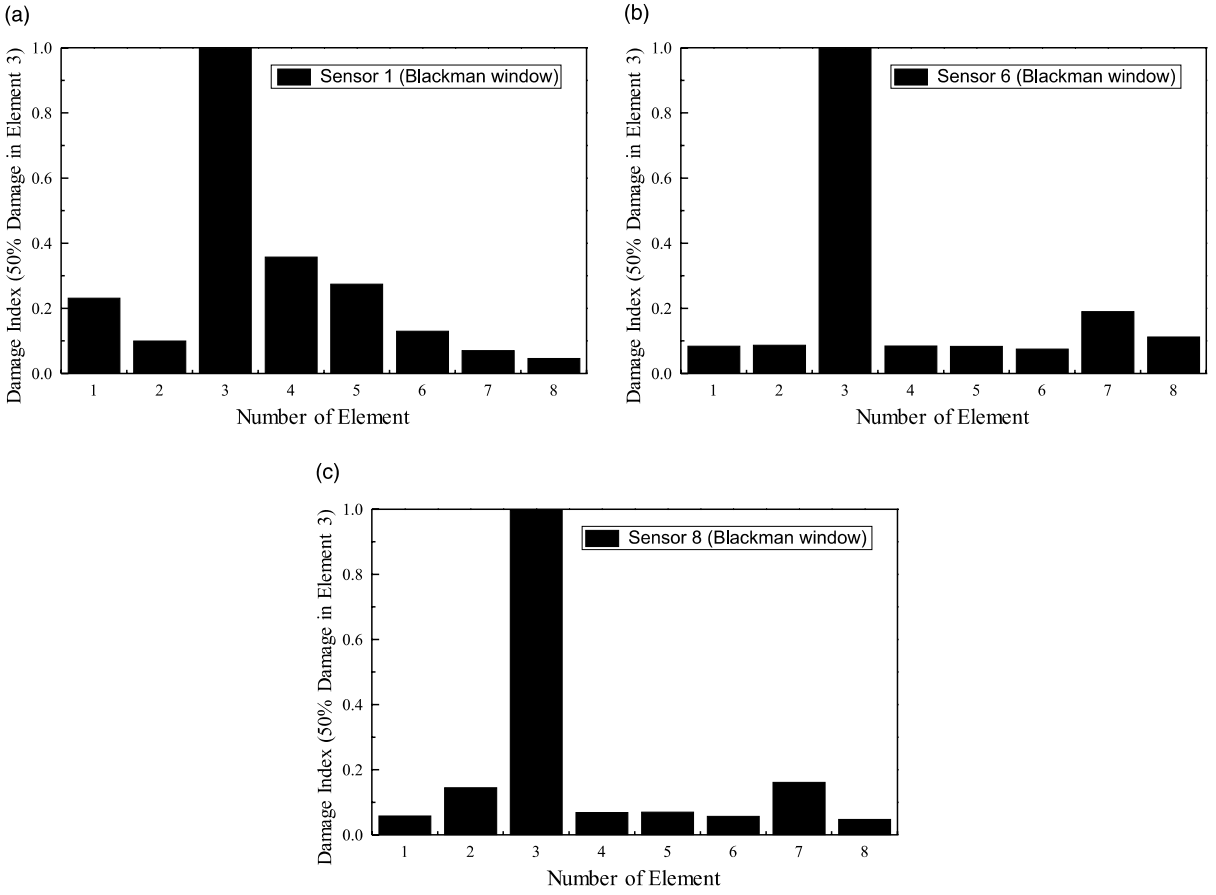

Fig. 15. Damage location using contaminated data on (a) sensor 1 (50% damage), (b) sensor 6 (50% damage), and (c) sensor 8 (50% damage).

Table 2
Results of damage extent (10% damage)

	Possible damaged element	Damage extent
Data of sensor 1	**3**	**−0.09844**
Data of sensor 6	**3**	**−0.09875**
Data of sensor 8	**3**	**−0.09863**

where

$$\varepsilon_x^0 = \frac{\partial u_0}{\partial x}, \qquad \varepsilon_y^0 = \frac{\partial v_0}{\partial y}, \qquad \varepsilon_{xy}^0 = \frac{\partial u_0}{\partial y} + \frac{\partial v_0}{\partial x} \tag{A.9}$$

$$\begin{aligned} \kappa_x^0 &= \frac{\partial \theta_x}{\partial x}, \qquad \kappa_y^0 = \frac{\partial \theta_y}{\partial y}, \qquad \kappa_{xy}^0 = \frac{\partial \theta_x}{\partial y} + \frac{\partial \theta_y}{\partial x} \\ \kappa_x^1 &= -\frac{4}{3h^2}\left(\frac{\partial \theta_x}{\partial x} + \frac{\partial^2 w}{\partial x^2}\right), \qquad \kappa_y^1 = -\frac{4}{3h^2}\left(\frac{\partial \theta_y}{\partial y} + \frac{\partial^2 w}{\partial y^2}\right) \end{aligned} \tag{A.10}$$

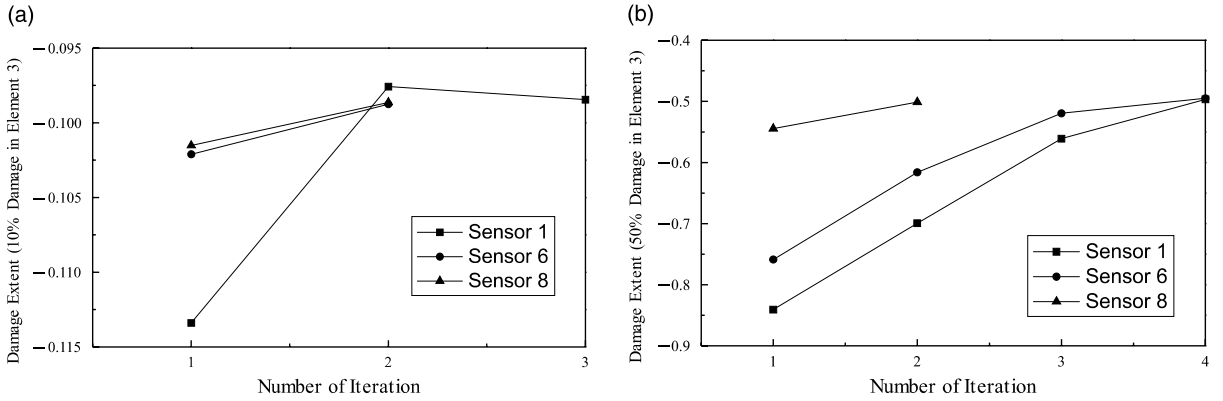

Fig. 16. Convergence history of damage extent: (a) 10% damage and (b) 50% damage.

Table 3
Results of damage extent (50% damage)

	Possible damaged element	Damage extent
Data of sensor 1	**3**	**−0.49674**
	3, 4, 5	**−0.49404**, 0.0, 0.0
	3, 1, 2, 4, 5, 6, 7, 8	**−0.49329**, 0.0,−0.00242, 0.0, 0.0, 0.0, 0.0, 0.0
Data of sensor 6	**3**	**−0.49507**
	3, 7, 8	**−0.49620**, 0.0, 0.0
	3, 1, 2, 4, 5, 6, 7, 8	**−0.49372**, 0.0, 0.0, 0.0, 0.0, 0.0, 0.0, 0.0
Data of sensor 8	**3**	**−0.50132**
	3, 2, 7	**−0.49643**, −0.00056, 0.0
	3, 1, 2, 4, 5, 6, 7, 8	**−0.49641**, 0.0, 0.0, 0.0, 0.0, 0.0, 0.0,−0.00006

$$\kappa_{xy}^1 = -\frac{4}{3h^2}\left(\frac{\partial\theta_x}{\partial y}+\frac{\partial\theta_y}{\partial x}+2\frac{\partial^2 w}{\partial x\,\partial y}\right) \tag{A.11}$$

$$\begin{aligned}&\varepsilon_{xz}^0 = \theta_x+\frac{\partial w}{\partial x}, \qquad \varepsilon_{yz}^0 = \theta_y+\frac{\partial w}{\partial y}\\ &\kappa_{xz}^1 = -\frac{4}{h^2}\left(\theta_x+\frac{\partial w}{\partial x}\right), \qquad \kappa_{yz}^1 = -\frac{4}{h^2}\left(\theta_y+\frac{\partial w}{\partial y}\right)\end{aligned} \tag{A.12}$$

The second-order derivatives of displacement in strains imply that elements of C^1-continuity are generally necessary. To derive a FEM using C^0-shape functions, two additional nodal degrees of freedom, i.e., $\boldsymbol{\chi} = \{\chi_x, \chi_y\}^{\mathrm{T}} = \{\partial w/\partial x, \partial w/\partial y\}^{\mathrm{T}}$ have been introduced. The nodal displacements are $\mathbf{u}_i^e = \{u_0^i, v_0^i, w_0^i, \theta_x^i, \theta_y^i, \chi_x^i, \chi_y^i\}^{\mathrm{T}}$. Then, the higher-order curvature and transverse shear terms in Eqs. (A.9)–(A.12) become as

$$\kappa_x^1 = -\frac{4}{3h^2}\left(\frac{\partial\theta_x}{\partial x}+\frac{\partial\chi_x}{\partial x}\right), \qquad \kappa_y^1 = -\frac{4}{3h^2}\left(\frac{\partial\theta_y}{\partial y}+\frac{\partial\chi_y}{\partial y}\right) \tag{A.13}$$

$$\kappa_{xy}^1 = -\frac{4}{3h^2}\left(\frac{\partial\theta_x}{\partial y}+\frac{\partial\theta_y}{\partial x}+\frac{\partial\chi_x}{\partial y}+\frac{\partial\chi_y}{\partial x}\right) \tag{A.14}$$

$$\varepsilon^0_{xz} = \theta_x + \chi_x, \qquad \varepsilon^0_{yz} = \theta_y + \chi_y \tag{A.15}$$

$$\kappa^1_{xz} = -\frac{4}{h^2}(\theta_x + \chi_x), \qquad \kappa^1_{yz} = -\frac{4}{h^2}(\theta_y + \chi_y) \tag{A.16}$$

The conditions $\psi_x = \chi_x - (\partial w/\partial x) = 0$ and $\psi_y = \chi_y - (\partial w/\partial y) = 0$ are enforced to be satisfied in the principle of virtual work using the penalty function method and selective reduced integration scheme. Then, the mechanical and electrical response of piezoelectrics can be obtained using the principle of virtual work to the equation of balance of momentum in the elastic field and the Maxwell's equation in the electric field as

$$\int_{S_e} \left[\delta\boldsymbol{\varepsilon}^{*\mathrm{T}} \mathbf{D}_c \boldsymbol{\varepsilon}^* - \delta\boldsymbol{\varepsilon}^{*\mathrm{T}} \overline{\mathbf{e}}^{*\mathrm{T}} \mathbf{E} - \delta\mathbf{E}^{\mathrm{T}} \overline{\mathbf{e}}^{*\mathrm{T}} \boldsymbol{\varepsilon}^* - \int_{-h/2}^{h/2} (\delta\mathbf{E}^{\mathrm{T}} \mathbf{p}\mathbf{E}) \mathrm{d}z + \int_{-h/2}^{h/2} (\delta\boldsymbol{\psi}^{\mathrm{T}} D_p \boldsymbol{\psi}) \mathrm{d}z + \int_{-h/2}^{h/2} (\rho\delta\mathbf{u}^{\mathrm{T}} \ddot{\mathbf{u}}) \mathrm{d}z \right] \mathrm{d}S - \delta W_u + \delta W_\phi = 0 \tag{A.17}$$

where S_e is the element area, $\mathbf{D}_c$ is the elastic matrix, $\overline{\mathbf{e}}^*$ is the piezoelectric coefficient matrix, $\mathbf{E}$ is the electric field vector which is equal to $-\nabla\boldsymbol{\phi}^e_S$, $\mathbf{p}$ is the dielectric matrix and the strain vector $\boldsymbol{\varepsilon}^* = \{\boldsymbol{\varepsilon}^0, \boldsymbol{\kappa}^0, \boldsymbol{\kappa}^1, \boldsymbol{\varepsilon}^0_s, \boldsymbol{\kappa}^1_s\}$, where $\boldsymbol{\varepsilon}^0 = \{\varepsilon^0_x, \varepsilon^0_y, \varepsilon^0_{xy}\}^{\mathrm{T}}$, $\boldsymbol{\kappa}^0 = \{\kappa^0_x, \kappa^0_y, \kappa^0_{xy}\}^{\mathrm{T}}$, $\boldsymbol{\kappa}^1 = \{\kappa^1_x, \kappa^1_y, \kappa^1_{xy}\}^{\mathrm{T}}$, $\boldsymbol{\varepsilon}^0_s = \{\varepsilon^0_{yz}, \varepsilon^0_{xz}\}^{\mathrm{T}}$ and $\boldsymbol{\kappa}^1_s = \{\kappa^1_{yz}, \kappa^1_{xz}\}^{\mathrm{T}}$. Also, in Eq. (A.17) there is $\boldsymbol{\psi} = \{\psi_x, \psi_y\}^{\mathrm{T}}$ and $\mathbf{D}_p$ is the penalty matrix including penalty parameters α_x and α_y as

$$\mathbf{D}_p = \begin{bmatrix} \alpha_x & 0 \\ 0 & \alpha_y \end{bmatrix} \tag{A.18}$$

Finally, the system equation can be written as

$$\begin{bmatrix} \mathbf{M}_{uu} & \mathbf{0} \\ \mathbf{0} & \mathbf{0} \end{bmatrix} \begin{Bmatrix} \ddot{\mathbf{u}} \\ \ddot{\boldsymbol{\phi}}_S \end{Bmatrix} + \begin{bmatrix} \mathbf{K}_{uu} & \mathbf{K}_{u\phi} \\ \mathbf{K}_{\phi u} & \mathbf{K}_{\phi\phi} \end{bmatrix} \begin{Bmatrix} \mathbf{u} \\ \boldsymbol{\phi}_S \end{Bmatrix} = \begin{Bmatrix} \mathbf{F}_u(t) \\ \mathbf{F}_\phi(t) \end{Bmatrix} \tag{A.19}$$

where the system matrices are assembled from the elemental matrices, which are

$$\mathbf{K}^e_{uu} = \mathbf{K}^e_{uk} + \mathbf{K}^e_{up} = \int_{-1}^{+1}\int_{-1}^{+1} \mathbf{B}_d^{\mathrm{T}} \mathbf{D}_c \mathbf{B}_d \det \mathbf{J} \, \mathrm{d}\xi \, \mathrm{d}\eta + \int_{-1}^{+1}\int_{-1}^{+1} \left(\int_{-h/2}^{h/2} \mathbf{B}_\psi^{\mathrm{T}} \mathbf{D}_p \mathbf{B}_\psi \, \mathrm{d}z \right) \det \mathbf{J} \, \mathrm{d}\xi \, \mathrm{d}\eta \tag{A.20}$$

$$\mathbf{K}^e_{u\phi} = \int_{-1}^{+1}\int_{-1}^{+1} \mathbf{B}_d^{\mathrm{T}} \overline{\mathbf{e}}^* \mathbf{B}_\phi \det \mathbf{J} \, \mathrm{d}\xi \, \mathrm{d}\eta \tag{A.21}$$

$$\mathbf{K}^e_{\phi\phi} = \int_{-1}^{+1}\int_{-1}^{+1} \left(\int_{-h/2}^{h/2} \mathbf{B}_\phi^{\mathrm{T}} \mathbf{p} \mathbf{B}_\phi \, \mathrm{d}z \right) \det \mathbf{J} \, \mathrm{d}\xi \, \mathrm{d}\eta \tag{A.22}$$

$$\mathbf{M}^e_{uu} = \int_{-1}^{+1}\int_{-1}^{+1} \left(\int_{-h/2}^{h/2} \rho \mathbf{N}^{\mathrm{T}} \mathbf{N} \, \mathrm{d}z \right) \det \mathbf{J} \, \mathrm{d}\xi \, \mathrm{d}\eta \tag{A.23}$$

Furthermore, the field variables are interpolated as follows:

$$\psi = \mathbf{B}_\psi \mathbf{u}^e, \quad \mathbf{E} = \mathbf{B}_\phi \boldsymbol{\phi}^e_S \text{ and } \boldsymbol{\varepsilon}^* = \mathbf{B}_d \mathbf{u}^e \tag{A.24}$$

The selective reduced integration scheme is used for the second term in Eq. (A.20), i.e., the penalty term, to overcome the possible locking phenomenon.

As a general condensation procedure, Eq. (A.19) can be cast into the following form:

$$\mathbf{M}_{uu}\ddot{\mathbf{u}} + \mathbf{K}^0\mathbf{u} = \mathbf{F}_u - \mathbf{F}_A \tag{A.25}$$

where the effective stiffness matrix $\mathbf{K}^0$ and actuator force vector $\mathbf{F}_A$ can be written as

$$\mathbf{K}^0 = \mathbf{K}_{uu} - \mathbf{K}_{u\phi}\mathbf{K}_{\phi\phi}^{-1}\mathbf{K}_{\phi u}, \qquad \mathbf{F}_A = \mathbf{K}_{u\phi}\boldsymbol{\phi}_A \tag{A.26}$$

The electric potential of sensors due to deformation can be obtained as

$$\boldsymbol{\phi}_S = -\mathbf{S}\mathbf{u} \text{ and } \mathbf{S} = \mathbf{K}_{\phi\phi}^{-1}\mathbf{K}_{\phi u} \tag{A.27}$$

It should be noted that structural damages only affect the matrix $\mathbf{K}_{uu}$.

References

Armon, D., Ben-Hain, Y., Braun, S., 1994. Crack detection in beams by rank-ordering of eigenfrequency shifts. Mechanical Systems and Signal Processing 8, 81–92.

Banks, H.T., Inman, D.J., Leo, D.J., et al., 1996. An experimentally validated damage detection theory in smart structures. Journal of Sound and Vibration 191, 859–880.

Chance, J., Tomlinson, G.R., Worden, K. 1994. A simplified approach to numerical and experimental modelling of the dynamics of cracked beam. Proceedings of the 12th International Modal Analysis Conference, 778–785.

Chandra, R., Singh, S.P., Gupta, K., 1999. Damping studies in fiber-reinforced composites – a review. Composite Structures 46, 41–51.

Cawley, P., Adams, R.D., 1979. The location of defects in structures from measurements of natural frequencies. Journal of Strain Analysis 14, 49–57.

Fukunaga, H., Hu, N., Ren, G.X., FEM modelling of adaptive composite structures using a higher-order plate theory. International Journal of Solids and Structures, in press.

Goldfarb, D., Idnani, A., 1983. A numerically stable dual method for solving strictly convex quadratic programs. Mathematical Programming 27, 1–33.

Jian, X.H., Tzou, H.S., Lissenden, C.J., et al., 1997. Damage detection by piezoelectric patches in a free vibration method. Journal of Composite Materials 31, 345–359.

Kahl, K., Sirkis, J.S., 1996. Damage detection in beam structures using subspace rotation algorithm with strain data. AIAA Journal 34, 2609–2614.

Keilers, C.H., Chang, F.K., 1995a. Identification delamination in composite beams using built-in piezoelectrics: Part I – Experimental and analysis. Journal of Intelligent Material Systems and Structures 6, 649–663.

Keilers, C.H., Chang, F.K., 1995b. Identification delamination in composite beams using built-in piezoelectrics: Part II – An identification method. Journal of Intelligent Material Systems and Structures 6, 664–672.

Luo, H., Hanagud, S., 1997. PVDF sensor and its application in delamination response detection. AIAA-97-1218, 720–729.

Okafor, A.C., Chandrashekhara, K., Jiang, Y.P., 1996. Delamination prediction in composite beams with built-in piezoelectric devices using modal analysis and neural network. Smart Materials and Structures 5, 338–347.

Oppenheim, A.V., Schafer, R.W., 1989. Discrete-Time Signal Processing. Prentice-Hall, Englewood Cliffs, NJ.

Penn, L.S., Jump, J.R., Greenfield, M.J., et al., 1999. Use of the free vibration spectrum to detect delamination in thick composites. Journal of Composite Materials 33, 54–72.

Schulz, M.J., Pai, P.F., Inman, D.J., 1999. Health monitoring and active control of composite structures using piezoceramic patches. Composites Part B 30, 713–725.

Schulz, M.J., Thyagarajian, S.K., 1995. Inverse dynamic design techniques for model correction and optimization. AIAA Journal 33, 1486–1491.

Stetson, K.A., 1975. Perturbation method of structural design relevant to holographic vibration analysis. AIAA Journal 13, 457–459.

Stubbs, N., 1987. A general theory of non-destructive damage detection in structures. Proceedings 2nd International Symposium on Structural Control, Edited by Leipholz, H. Netherlands, pp. 694–713.

Wang, X., Hu, N., Fukunaga, H., et al., 2001. Structural damage identification using static test data and changes in frequencies. Engineering Structures 23, 610–621.

Wang, Z., Lin, R.M., Lim, M.K., 1997. Structural damage detection using measured FRF data. Computer Methods in Applied Mechanics and Engineering 147, 187–197.

Weissenburger, J.T., 1968. Effect of local modifications on the vibration characteristics of linear systems. Journal of Applied Mechanics 35, 327–332.

Zou, Y., Tong, L., Steven, G.P., 2000. Vibration-based model-dependent damage (delamination) identification and health monitoring for composite structures – a review. Journal of Sound and Vibration 230, 357–378.